Basic elements for simulations of standard-model physics with quantum annealers: Multigrid and clock states

Marc Illa* and Martin J. Savage†
InQubator for Quantum Simulation, Department of Physics, University of Washington, Seattle, Washington 98195, USA

(Received 21 March 2022; accepted 26 October 2022; published 14 November 2022)

We explore the potential of D-Wave's quantum annealers for computing some of the basic components required for quantum simulations of standard model physics. By implementing a basic multigrid (including "zooming") and specializing Feynman-clock algorithms, D-Wave's Advantage is used to study harmonic and anharmonic oscillators relevant for lattice scalar field theories and effective field theories, the time evolution of a single plaquette of SU(3) Yang-Mills lattice gauge field theory, and the dynamics of flavor entanglement in four-neutrino systems.

DOI: 10.1103/PhysRevA.106.052605

I. INTRODUCTION

Simulations of the dynamics of quantum matter, from neutron stars to materials, which are beyond the reach of classical computation, are expected to become possible through continued advances in quantum computation. While universal quantum computation [1–8] is essential in this quest to simulate standard-model physics, the near-term devices that define the noisy intermediate-scale quantum (NISQ) era [9], without high-fidelity qubits and error correction, will be challenged to provide results that can be quantitatively compared with experiment (see, for example, Refs. [10–12]). Much of the current research in this area is performed on gate-based quantum computers, and the alternative adiabatic quantum computing [13–16] has not been explored with as much detail. Applications for such devices, such as D-Wave's quantum annealers (QAs) [17–19], are optimization [20–25], high-energy physics [26,27], machine learning [28–40], spin systems [41–51], quantum chemistry [52–57], biology [58–61], finance [62–64], graph equations [65–67], multivariate equations [68], integer equations [69], linear equations [70], and factorization problems [71–76], and more, but a quantum advantage for scientific applications remains to be demonstrated.

The first steps toward simulating quantum field theories using QAs have been taken by finding the ground state of modest SU(2) plaquette systems and the time evolution of these systems [77] using the Feynman-clock algorithm [78]. Given that, modulo emergent fine-tunings, many standard-model systems of interest are gapped, with finite correlation lengths, quantum circuits for universal quantum computers are expected to be able to have localized control structures for which domain decomposition will be effective. This suggests that QAs may provide efficient preconditioners for preparing parametrizations of ground states and excited states for universal quantum computers (e.g., fast-forwarding time evolution [79]) in the future. This of course remains to be demonstrated.

Using D-Wave's QAs (and simulators), we explore building blocks that are required for quantum simulations of standard-model physics and its descendant low-energy effective field theories. Building upon the works of Refs. [70,77], a "zooming" algorithm is used to converge coefficients of the basis states defining annealing problem instances for ground states. Second, we use a simple multigrid procedure that iteratively employs course grids to provide starting conditions for finer grids to converge wave functions. Third, we generalize a previously implemented Feynman-clock algorithm [77] to arbitrary Hermitian matrices. These algorithms are used to simulate the harmonic oscillators (HOs) and anharmonic oscillators (AHOs), the time evolution of the SU(3) Yang-Mills plaquette [80], and neutrino flavor evolution [81], which have been previously simulated using IBM's superconducting quantum computers.

II. MAPPING A HAMILTONIAN ONTO A QUADRATIC UNCONSTRAINED BINARY OPTIMIZATION PROBLEM

In order to find the ground-state energy and wave function of a given Hamiltonian using D-Wave's QAs, a minimization problem is mapped onto a quadratic unconstrained binary optimization (QUBO) problem $f_Q(q) = \sum_{ij} Q_{ij} q_i q_j$, where q_i are binary variables. Following techniques and protocols for using D-Wave's systems [82] and specific methods that users have developed [55,77], an objective function of the form

$$F = \langle\Psi|\hat{\mathcal{H}}|\Psi\rangle - \eta\langle\Psi|\Psi\rangle \tag{1}$$

is minimized, where η is a parameter that is tuned to avoid the null solution ($\langle\Psi|\Psi\rangle = 0$). Expanding or approximating the wave function $|\Psi\rangle$ in a finite-dimensional orthonormal basis $|\psi_\alpha\rangle$, $|\Psi\rangle = \sum_\alpha^{n_s} a_\alpha |\psi_\alpha\rangle$, with a_α real numbers, F can

*marcilla@uw.edu
†mjs5@uw.edu

be written as

$$F = \sum_{\alpha\beta}^{n_s} a_\alpha a_\beta (\langle\psi_\alpha|\hat{\mathcal{H}}|\psi_\beta\rangle - \eta\langle\psi_\alpha|\psi_\beta\rangle)$$
$$= \sum_{\alpha\beta}^{n_s} a_\alpha a_\beta (\hat{\mathcal{H}}_{\alpha\beta} - \eta\delta_{\alpha\beta}) = \sum_{\alpha\beta}^{n_s} a_\alpha a_\beta h_{\alpha\beta}. \quad (2)$$

Mapping the minimization of F onto a QUBO problem appropriate for solution using an annealer requires expressing a_α in terms of binary variables. Following previous works, the fixed-point representation [55] of each a_α in terms of K bits q_i^α is used,

$$a_\alpha = -q_K^\alpha + \sum_{i=1}^{K-1} \frac{q_i^\alpha}{2^{K-i}}, \quad (3)$$

where $a_\alpha \in [-1, 1)$. Finer digitizations of a_α, accomplished by the use of larger values of K, provide better resolution of the a_α and consequently higher precision and accuracy in solution, but are limited by device performance with increasing size of the QUBO matrix. This digitization of a_α puts the expression in Eq. (2) into QUBO form

$$F = \sum_{\alpha\beta,ij} Q_{\alpha,i;\beta,j} q_i^\alpha q_j^\beta, \quad (4)$$

with $Q_{\alpha,i;\beta,j} = 2^{i+j-2K}(-1)^{\delta_{iK}+\delta_{jK}} h_{\alpha\beta}$. The QUBO matrix $Q_{\alpha,i;\beta,j}$, with dimensions $Kn_s \times Kn_s$, is subsequently passed from the D-Wave application programming interface to a simulator or D-Wave's QAs.

An adaptive QA eigenvalue (AQAE) solver, implemented in Refs. [70,77], incorporates an algorithmic improvement that reduces the required value of K to reach a given solve precision and hence increases the size of problem instances that can be addressed using any given QA (a similar idea was applied in Ref. [83] for machine learning). After the initial solve for coefficients $a_\alpha^{(z=0)}$, the range of search values for $a_\alpha^{(z+1)}$ are systematically reduced, guided by the previously obtained $a_\alpha^{(z)}$. This permits not only a reduced value for K but also a reduced number of anneals at each zoom level. We implement a relation between successive zoom steps similar to Ref. [70], of the form

$$a_\alpha^{(z+1)} = a_\alpha^{(z)} - 2^{-z} q_K^\alpha + \sum_{i=1}^{K-1} \frac{q_i^\alpha}{2^{K-i+z}}. \quad (5)$$

An example of the progressive decimation of a coefficient $a_\alpha^{(z+1)}$ with increasing zoom step is shown in Fig. 1. In forming the QUBO matrix at each zoom step, the contributions that are naively linear in q_i^α in the product $a_\alpha^{(z+1)} a_\beta^{(z+1)}$ are changed to quadratic via $q_i^\alpha = (q_i^\alpha)^2$. The derivation of the QUBO matrix can be found in Appendix A, yielding

$$Q_{\alpha,i;\beta,j} = 2^{i+j-2K-2z}(-1)^{\delta_{iK}+\delta_{jK}} h_{\alpha\beta}$$
$$+ 2\delta_{\alpha\beta}\delta_{ij} 2^{i-K-z}(-1)^{\delta_{iK}} \sum_\gamma a_\gamma^{(z)} h_{\gamma\beta}. \quad (6)$$

As considered in Ref. [56], excited states can also be addressed with this same construction by including chemical potentials for the states that are lower in the spectrum. The

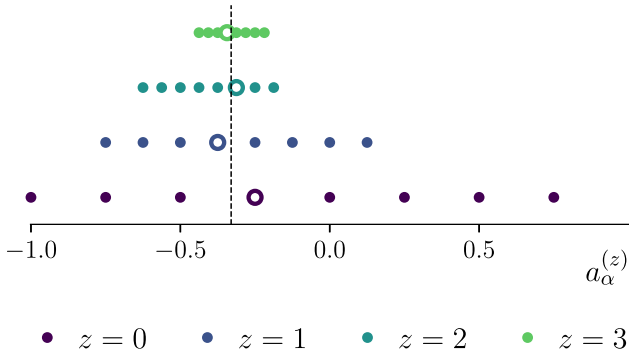

FIG. 1. Example of the convergence of $a_\alpha^{(z)}$ from the iterative zooming method discussed in the text using $K = 3$, for a true value of $a_\alpha = -0.33$ (vertical dashed line). The closed circles denote the sampled values of $a_\alpha^{(z)}$ at each zoom step. The open circles correspond to the points closest to the true value of a_α and are used as input for the subsequent zoom step.

Nth state in the spectrum can be obtained by including $N-1$ chemical potentials μ_n that give an energy shift to each of the nth states that place them higher in the spectrum than the Nth state. To accomplish this, an effective Hamiltonian of the form

$$\hat{\mathcal{H}}^{(N)} = \hat{\mathcal{H}} + \sum_n^{N-1} \mu_n |\Psi_n\rangle\langle\Psi_n| \quad (7)$$

is used. The μ_n depend upon the energy eigenvalues of $|\Psi_{n<N}\rangle$, both of which are determined in earlier problem solutions using $\mathcal{H}^{(n<N)}$ in the workflow, and an approximate knowledge of the energy of $|\Psi_N\rangle$, determined possibly in tuning or from other approximate solutions. Explicitly, to implement Eq. (7) and find the $(n+1)$th excited state, the wave functions of the nth lowest-lying states are used to generate a matrix contribution from the outer products $|\Psi_n\rangle\langle\Psi_n|$, which are multiplied by μ_n and added to the existing Hamiltonian (see the Supplemental Material [84] for the practical implementation of these and subsequent algorithms).

Analyzing results from annealing simulator and quantum devices

For any given QUBO matrix, annealing simulators or QAs perform N_A anneals to locate the lowest-energy configuration(s) and associated wave function(s). Outputs of the annealing workflow include an ensemble of N_A results, and generation of such ensembles can be repeated N_{run} times to provide estimates of associated uncertainties. As the lowest-energy configuration in an ensemble provides the lowest upper bound to the true energy of the target state, N_{run} sets of such measurements can yield a global minimum energy and wave function, and also a mean and standard deviation, or a median and 68% confidence interval (for robustness). These estimators provide a measure of some uncertainties, including those associated with zooming and fluctuations in the annealing process.

Systematic studies of uncertainties associated with D-Wave's QAs have been previously performed, e.g., Refs. [85–87]. These contain detailed sets of measurements

and discussions of device configuration and noise. The D-Wave online documentation [88], in particular that related to D-Wave's quantum simulator neal, provides algorithms to simulate the annealers, discussions of the noise model, and provides codes.

To differentiate between results obtained with a noisy simulator and a QA that are shown in figures in the text, we will assign one of the icons introduced in Ref. [89]: the yellow square icon for results obtained using neal and the blue diamond icon for those obtained using D-Wave's QA Advantage system 4.1 (which we will refer to simply as Advantage).

III. HARMONIC AND ANHARMONIC OSCILLATORS: EIGENSTATES AND ENERGIES

Perhaps the simplest quantum field theory to consider is $\lambda\phi^4$ scalar field theory. Jordan *et al.* have shown that state preparation and simulating S-matrix elements resides in the BQP-complete complexity class [90]. As a starting point for exploring lattice scalar field theory using QAs, we examine a single-site harmonic oscillator with and without the nonlinear $\lambda\phi^4$ interaction. The Hamiltonian for a single site has the form

$$\hat{\mathcal{H}} = \frac{1}{2}\hat{\Pi}^2 + \frac{1}{2}m_0^2\hat{\phi}^2 + \frac{\lambda}{4!}\hat{\phi}^4, \tag{8}$$

with the bare mass m_0 and bare coupling λ [all quantities are in lattice units (l.u.)]. In the Jordan-Lee-Preskill (JLP) basis [90–94], the field ϕ is digitized at each spatial site in a space spanned by n_s uniformly distributed states[1] with mapped values

$$\phi = -\phi_{\max} + \delta_\phi\beta_\phi, \quad \delta_\phi = \frac{2\phi_{\max}}{n_s - 1}, \tag{9}$$

where $\phi_{\max}$ is the maximum value of $\phi(\mathbf{x})$ and $\beta_\phi = 0, 1, \ldots, n_s - 1$. In ϕ space, while two of the terms in Eq. (8) are diagonal, the conjugate momentum operator can be computed with a finite-difference operator. However, this introduces polynomial δ_ϕ-discretization errors. A better way to compute it is to use quantum Fourier transforms into and out of conjugate momentum space [91,92], since $\langle k_\phi|\hat{\Pi}^2|k'_\phi\rangle = k_\phi^2\delta_{k_\phi,k'_\phi}$, with

$$k_\phi = -k_\phi^{\max} + \left(\beta_\phi - \frac{1}{2}\right)\delta k_\phi,$$
$$k_\phi^{\max} = \frac{\pi}{\delta_\phi}, \quad \delta k_\phi = \frac{2\pi}{\delta_\phi n_s}. \tag{10}$$

This has been shown to eliminate power-law corrections to $\hat{\Pi}^2$, giving exponentially convergent digitization via the Nyquist-Shannon theorem [90–98]. A detailed comparison between this operator and finite-difference versions can be found in an Appendix of Ref. [94]. For a given number of states n_s, the Hamiltonian is an $n_s \times n_s$ real matrix, from which the eigenstates and energies can be found via mappings to a QUBO problem and annealing, as discussed in Sec. II.

[1]For a register of a universal quantum computer of n_Q qubits, $n_s = 2^{n_Q}$.

A. Results from the annealer simulator neal

Available D-Wave annealer simulators were used to prepare for working with D-Wave's cloud-accessible QAs. In particular, for the one-site system, the simulator was used to perform parameter tunings and calibrations, including the maximum and minimum values of the field $\phi_{\max}$, the number of states over which the field is digitized n_s, η in the objective function [in Eq. (1)], the chemical potentials μ_n [in Eq. (7)], the number of qubits per coefficient K, the number of anneals per zoom step N_A, and the total number of zoom steps $z^{\max}$. These identified values, or initial tunings, for these parameters, and measures of uncertainties, both systematic and statistical, are a subset of those that will be present for computations using QAs. Our workflow for the simulator and quantum hardware was implemented with PYTHON [99] using JUPYTER notebooks [100] after formulating the matrix problem with *Mathematica* [101].

1. Tunings

We present only highlights of parameter tunings as they generally behave as naively anticipated or as determined previously. Figure 2(a) shows the systematic deviation from the true digitized ground-state energy of the HO determined using the annealing simulator for $m_0 = 1$, $\lambda = 0$, and $\phi_{\max} = 5$ digitized across $n_s = 32$ states as a function of η for $N_A = 10^3$ and $K = 3$. The solid lines with points correspond to minimum-energy solutions, while the solid bands correspond to the 68% confidence intervals determined from $N_{\text{run}} = 200$ samples. The accuracy in the energy is found to be optimized for $\eta \sim E_0$. Figure 2(b) shows the deviations in energy for different levels of zooming as a function of N_A for $K = 3$ and $\eta = 0.51$. While the minimum-energy estimate is improved with an increasing number of anneals, increasing the zoom level leads to a more rapid convergence. Similarly, Fig. 2(c) shows the energy deviation as a function of K for different levels of zoom for $N_A = 10^3$ and $\eta = 0.51$. Although larger values of K can increase the precision of the ground-state energy, as is the case for N_A, using more zoom steps can also reach similar levels (without increasing the number of qubits). Overall conclusions from these explorations of parameter space are that η should be close to the energy of the ground state and that the use of "sloppy solutions," where a relatively small number of anneals N_A are used to iteratively estimate subsequent zoom intervals for QUBO parameters, can be used to make efficient use of computational resources.[2] We consider it to be somewhat unfortunate that the dependence on η is that shown in Fig. 2(a), as ideally quantities would be independent of η.

The systematic improvements in results with increasing N_A, K, and number of zoom levels using the annealer simulator do not persist indefinitely, which is attributed to the white noise intrinsic to neal.

[2]The latter technique is in the spirit of all-mode averaging techniques employed in some lattice quantum chromodynamics generations of light quark propagators, e.g., Refs. [102,103].

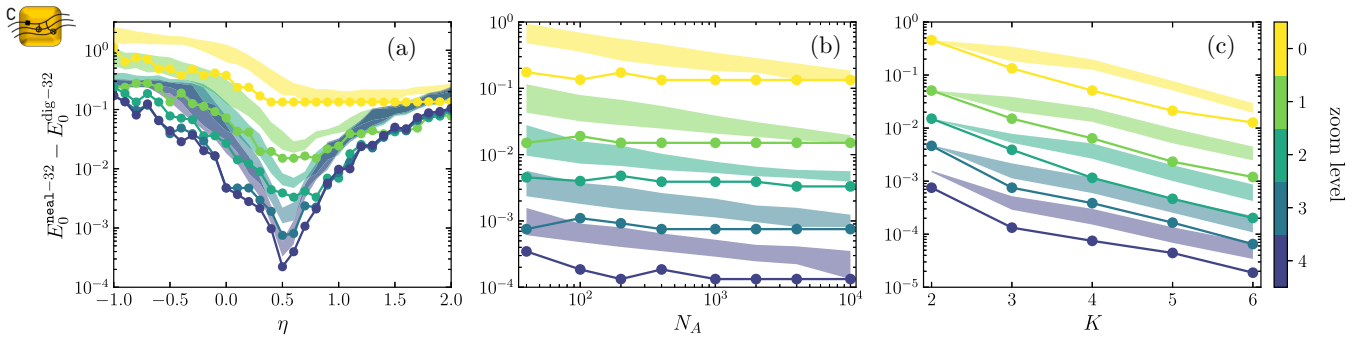

FIG. 2. Ground-state energy (in l.u.) of the HO obtained with D-Wave's neal as a function of (a) the parameter η, (b) the number of anneals N_A, and (c) the parameter K, for $m_0 = 1$, $\lambda = 0$, and $\phi_{\max} = 5$ discretized across $n_s = 32$ states, setting $\eta = 0.51$, $N_A = 10^3$, and $K = 3$ when the corresponding parameter is not varied. The solid lines with points correspond to minimum-energy solutions, while the solid bands correspond to the 68% confidence intervals determined from $N_{\mathrm{run}} = 200$ independent runs of the annealing workflow.

2. *Harmonic oscillator:* $V(\phi) = \frac{1}{2}\phi^2$

For demonstrative purposes, through the use of appropriately tuned parameters, we present the results for the lowest six eigenstates of the HO with $V(\phi) = \frac{1}{2}\phi^2$ (i.e., $m_0 = 1$). The exact energies in the field-space continuum limit are $E_n^{\mathrm{exact}} = \{\frac{1}{2}, \frac{3}{2}, \frac{5}{2}, \frac{7}{2}, \frac{9}{2}, \frac{11}{2}, \ldots\}$, with eigenfunctions given by

$$\Psi_n(\phi) = \frac{1}{\sqrt{2^n n!}}\left(\frac{1}{\pi}\right)^{1/4} e^{-(1/2)\phi^2} H_n(\phi), \tag{11}$$

where $H_n(x)$ are the Hermite polynomials. A systematic study of the impact of digitization on the low-lying wave functions and energies has been performed previously [94] and we use that as a guide in selecting digitization parameters. We work with $\phi_{\max} = 5$ and $n_s = 64$, resulting in $\delta\phi = 0.1587$ and $k_{\max} = 19.7920$, and energies $E_{n\leqslant 6}^{\mathrm{dig}-64}$ that are the same as $E_{n\leqslant 6}^{\mathrm{exact}}$ to better than approximately 10^{-5}. The value of η_n was set equal to the corresponding $E_n^{\mathrm{exact}} + 0.01$, and the chemical potentials were set to $\mu_n = 10$ when appropriate, to move each of the previously determined states to an energy higher than the "next" ground state. The energies of the lowest states found using neal are given in Table I and displayed in Figs. 3(a) and 3(d) (with $N_A = 10^3$) and recover the digitized values with accuracy of approximately 10^{-3}–10^{-6}.

TABLE I. Energies associated with the HO with $m_0 = 1$ (in l.u.). The exact energies are shown in the second column, the difference between the diagonalization of the digitized Hamiltonian and exact energies are shown in the third column, with $\phi_{\max} = 5$ and $n_s = 64$, and the differences between the digitized energies and the corresponding results obtained using D-Wave's annealer simulator neal are shown in the fourth (no MG) and fifth (with MG) columns, with the uncertainties showing the 68% confidence intervals, with $K = 3$ and $N_A = 10^3$.

n	E_n^{exact}	$\lvert\delta E_n^{\mathrm{dig}-64}\rvert$	$\lvert\delta E_n^{\mathrm{neal}-64}\rvert_{z=0}$	$\lvert\delta E_n^{\mathrm{neal}-64}\rvert_{z=8}$
0	1/2	3.5×10^{-11}	$(4.9^{+2.5}_{-1.8}) \times 10^{-6}$	$(4.0^{+2.6}_{-1.2}) \times 10^{-6}$
1	3/2	1.8×10^{-9}	$(9.1^{+409}_{-5.1}) \times 10^{-6}$	$(5.2^{+2.5}_{-1.7}) \times 10^{-6}$
2	5/2	4.1×10^{-8}	$(4.7^{+4.7}_{-2.0}) \times 10^{-6}$	$(4.4^{+2.2}_{-1.6}) \times 10^{-6}$
3	7/2	6.6×10^{-7}	$(0.7^{+200}_{-0.3}) \times 10^{-5}$	$(5.3^{+2.7}_{-1.6}) \times 10^{-6}$
4	9/2	6.6×10^{-6}	$(5.5^{+7.2}_{-2.0}) \times 10^{-6}$	$(4.4^{+2.1}_{-1.6}) \times 10^{-6}$
5	11/2	6.0×10^{-5}	$(0.7^{+100}_{-0.3}) \times 10^{-5}$	$(4.7^{+2.3}_{-1.6}) \times 10^{-6}$

In order to reduce the uncertainty bands, instead of increasing N_A or K, we work with a (somewhat basic) multigrid (MG) AQAE solver, inspired by the wide success of multigrid algorithms [104], where a coarser (smaller) system is solved first and that solution is used as an input parameter for the finer (larger) system. Specific to our case, a coarser system can be defined by using a smaller value of n_s for the digitization of the field. With the coefficients $a_\alpha^{(z)}$ extracted from the $n_s = 32$ system, we interpolate (using cubic splines) to find starting points for the $n_s = 64$ system. To help guide the annealer, it has been found that starting with $z^{\mathrm{init}} \gtrsim 4$ reduces the uncertainty on the energies, as it limits the range of the values that $a_\alpha^{(z)}$ can assume. As shown in Figs. 3(b), 3(c), 3(e), and 3(f), starting with $z^{\mathrm{init}} = 4$ or 8 significantly reduces the error compared to $z^{\mathrm{init}} = 0$.

To display the convergence obtained with neal for an increasing number of zoom steps, Figs. 3(a)–3(c) show the deviation in the energy of the lowest six states as a function of zoom steps. The convergence is consistent with exponential in the number of zoom steps, as found in Ref. [70]. This result is encouraging as the HO is one of the simplest systems to consider.

The wave functions associated with the energies in Table I are shown in Figs. 3(d)–3(f). The diagonalization of the HO employed $\phi_{\max} = 5$, $n_s = 64$, and $m_0 = 1$ and reproduced the values of the continuum-field wave functions with high precision, a well-known result. For the ground state, the digitized wave function (squares) reproduces the continuum wave function to better than approximately 10^{-6}, as shown in Fig. 4. Using neal, $K = 3$ and $\eta = 0.51$ were used with 14 levels of zoom. The wave functions, shown by the lines in Fig. 3, reproduce the digitized wave functions to better than approximately 10^{-3}, as shown for the ground state in Fig. 4. Similar fidelity is obtained for the other wave functions.

Overall, the HO is amenable to simulation with neal. With appropriate (and easy to identify) parameter tunings, the energies and wave functions of the lowest-lying states can be determined with precision. Results for coarser and finer digitizations behave in ways that are consistent with expectations. While we have not performed a systematic exploration, we

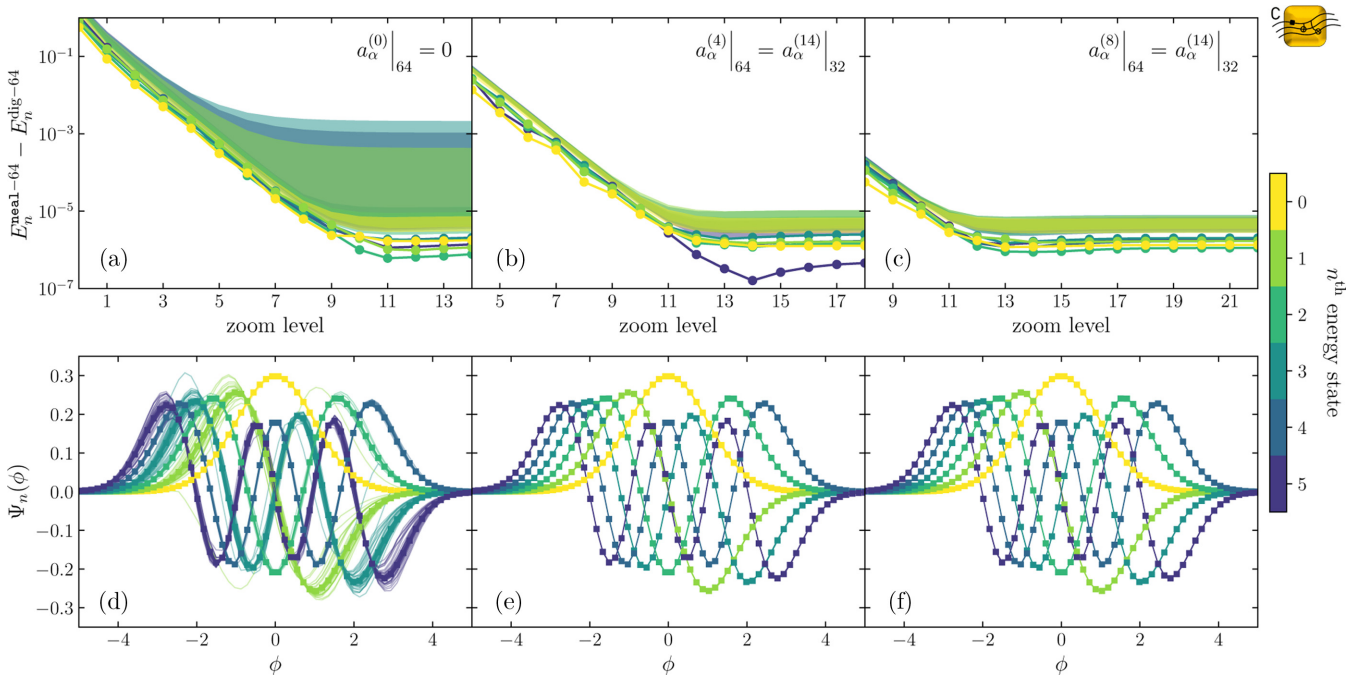

FIG. 3. (a)–(c) Convergence of the energy (in l.u.) of the first six HO states as a function of the number of zoom steps, where the solid lines with points correspond to minimum-energy solutions, while the solid bands correspond to the 68% confidence intervals determined from $N_{\mathrm{run}} = 200$ independent runs of the annealing workflow. (d)–(f) Lowest six HO wave functions [multiplied by $(-1)^n$]. The squares denote the exact values from the digitized Hamiltonian, while the lines show the $N_{\mathrm{run}} = 200$ independent runs obtained using D-Wave's annealer simulator neal with the maximal number of zoom steps. The results from neal are also sets of discrete points, and for display purposes we have shown them as joined line segments. The initial coefficients for (a) and (d) are null coefficients, for (b) and (e) correspond to starting the $z^{\mathrm{init}} = 4$ zooming for $n_s = 64$ states from the $z^{\mathrm{max}} = 14$ values and their interpolations from $n_s = 32$, and for (c) and (f) correspond to starting with $z^{\mathrm{init}} = 8$. The maximum value of the field is $\phi_{\mathrm{max}} = 5$ digitized on $n_s = 64$ states, with $K = 3$ and $N_A = 10^3$.

expect that the primary limitation on the number of states of the HO that can be isolated with precision is the accumulation of errors through the iterative process of Eq. (7).

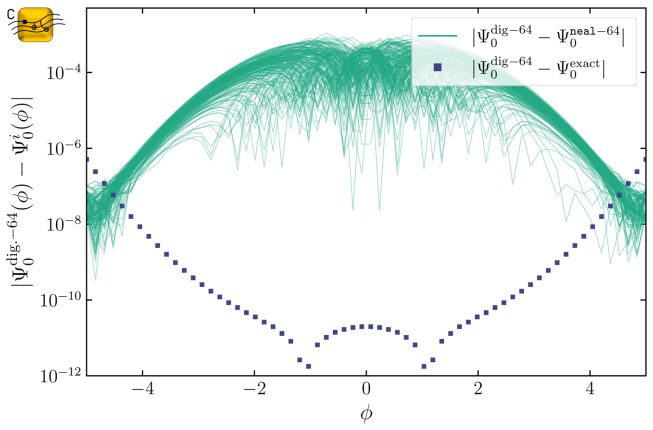

FIG. 4. Deviations between the digitized ground-state HO wave function and the analytic continuum-field expression (squares) and the wave functions determined using neal (lines, showing the $N_{\mathrm{run}} = 200$ independent runs). The digitized simulation employed $\phi_{\mathrm{max}} = 5$, $n_s = 64$, $m_0 = 1$, $K = 3$, $\eta = 0.51$, $N_A = 10^3$, and $\{z^{\mathrm{init}}, z^{\mathrm{max}}\} = \{8, 22\}$.

3. *Anharmonic oscillator:* $V(\phi) = \frac{1}{2}\phi^2 + \frac{4}{3}\phi^4$

Depending upon the size of the nonlinear interaction, the low-lying spectrum of the AHO can differ significantly from those of the HO. For the coupling of $\lambda = 32$ that we have chosen for demonstrative purposes, important differences are present in both the energy and wave functions of the one-site system. The value of η_n used to solve for nth eigenstate is set, as in the HO case, to the corresponding $E_n^{\mathrm{exact}} + 0.01$, the chemical potentials are set to $\mu_n = 20$, $K = 3$, and the number of anneals is $N_A = 10^3$. Table II displays the exact energies, the difference between the exact and digitized energies for the system with $\phi_{\mathrm{max}} = 2.6$ and $n_s = 64$, and the difference between the results obtained using neal and the exact digitized energies.

The convergence of the energy of the lowest-lying states with increasing numbers of zoom steps determined using neal are shown in Figs. 5(a)–5(c), with exponential convergence seen up to approximately 12 zoom steps, beyond which there are diminishing returns. The converged wave functions for each level are shown in Figs. 5(d)–5(f). As in the case of the HO, the MG AQAE method reduces the uncertainties in the extracted energies. Further, the wave functions converge well to the exact digitized wave functions (shown as the squares in Fig. 5). Figures 5(d)–5(f) show the wave functions resulting from $N_A = 10^3$ anneals compared to the exact result.

TABLE II. Energies associated with the AHO with $m_0 = 1$ and $\lambda = 32$ (in l.u.). The exact energies are shown in the second column, the difference between the diagonalization of the digitized Hamiltonian and exact energies are shown in the third column, with $\phi_{\max} = 2.6$ and $n_s = 64$, and the differences between the digitized energies and the corresponding results obtained using D-Wave's annealer simulator neal are shown in the fourth (no MG) and fifth (with MG) columns, with the uncertainties showing the 68% confidence intervals, with $K = 3$ and $N_A = 10^3$.

n	E_n^{exact}	$\lvert\delta E_n^{\text{dig}-64}\rvert$	$\lvert\delta E_n^{\text{neal}-64}\rvert_{z=0}$	$\lvert\delta E_n^{\text{neal}-64}\rvert_{z=8}$
0	0.8597427	1.7×10^{-9}	$(0.9^{+223}_{-0.8}) \times 10^{-5}$	$(1.7^{+1.1}_{-0.7}) \times 10^{-6}$
1	2.9493637	2.4×10^{-8}	$(0.5^{+239}_{-0.5}) \times 10^{-4}$	$(1.8^{+1.6}_{-0.6}) \times 10^{-6}$
2	5.6096611	2.0×10^{-7}	$(0.2^{+161}_{-0.1}) \times 10^{-5}$	$(1.2^{+0.7}_{-0.6}) \times 10^{-6}$
3	8.6270258	1.5×10^{-6}	$(0.5^{+279}_{-0.3}) \times 10^{-5}$	$(2.7^{+1.6}_{-0.7}) \times 10^{-6}$
4	11.930637	8.0×10^{-6}	$(0.2^{+782}_{-0.1}) \times 10^{-5}$	$(1.4^{+0.7}_{-0.4}) \times 10^{-6}$
5	15.476155	4.4×10^{-5}	$(4.1^{+439}_{-4.1}) \times 10^{-4}$	$(3.0^{+1.6}_{-1.0}) \times 10^{-6}$

B. Implementations and results from D-Wave annealers

We have run the codes used in Sec. III A with neal on D-Wave's QA Advantage, which has 5627 physical qubits, and each qubit is connected with 15 other qubits (in a so-called Pegasus topology). The system is accessible through the cloud via D-Wave's website [105].

The mapping between the QUBO problem and the processor topology is performed automatically, via heuristics algorithms [106], and is the most time-consuming part of the simulation, as discussed in Appendix B (the embedding can be computed at the beginning and it also can be reused for all the zoom steps). During this process, as there is no all-to-all connectivity, several physical qubits are chained together to form a logical qubit with the required connectivity. To enforce that the qubits in a certain chain have all the same value, an extra parameter, the chain-strength value c_s, is fixed. As the elements of the QUBO matrix are rescaled to lie in the range $[-1, 1]$ when they are passed to Advantage, if $c_s \gg \max(|Q|)$, the QUBO elements will be rescaled closer to zero. We set $c_s = \omega \max(|Q|)$ and scan over $\omega \in [0, 1]$, finding that $\omega = 0.2$ gives the lowest energies for these systems. Another parameter that can be tuned is the annealing schedule and annealing time t_A and we have used its default value of $t_A = 20\ \mu$s in our calculations. It has been previously observed, e.g., Ref. [63], that using different annealing schedules, like reverse annealing, can increase the success rate (finding the solution with minimum energy) of the QA. The exploration of such improvements is left for future work. Due to Advantage's intrinsic noise, extracting energies and wave functions with adequate precision for $n_s \geqslant 16$ requires using the MG AQAE solver. Compared to the neal simulator, a smaller initial value of $n_s = 16$ is required for Advantage to provide meaningful results. These results are then used as starting values for the

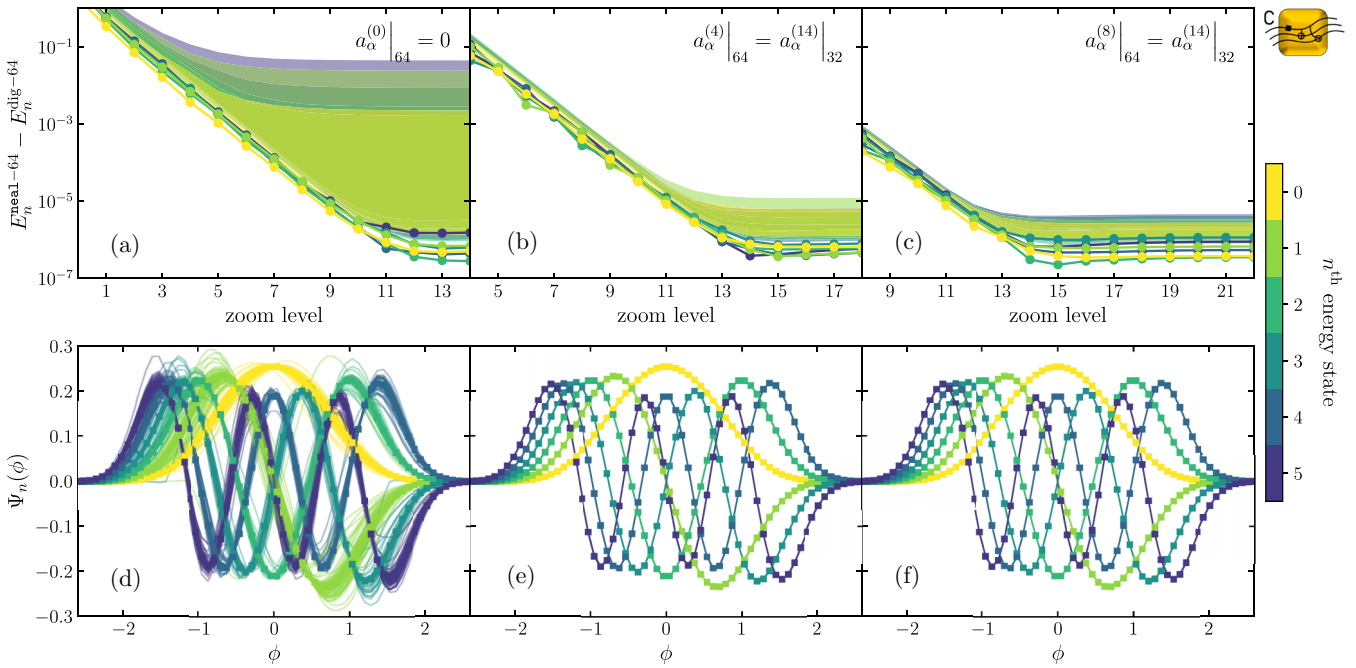

FIG. 5. (a)–(c) Convergence of the energy (in l.u.) of the first six AHO states as a function of the number of zoom steps, where the solid lines with points correspond to minimum-energy solutions, while the solid bands correspond to the 68% confidence intervals determined from $N_{\text{run}} = 200$ independent runs of the annealing workflow. (d)–(f) Lowest six AHO wave functions [multiplied by $(-1)^n$]. The squares denote the exact values from the digitized Hamiltonian, while the lines show the $N_{\text{run}} = 200$ independent runs obtained using D-Wave's annealer simulator neal with the maximal number of zoom steps. The initial coefficients for (a) and (d) are null coefficients, for (b) and (e) correspond to starting the $z^{\text{init}} = 4$ zooming for $n_s = 64$ states from the $z^{\max} = 14$ values and their interpolations from $n_s = 32$, and for (c) and (f) correspond to starting with $z^{\text{init}} = 8$. The maximum value of the field is $\phi_{\max} = 2.6$ digitized on $n_s = 64$ states, with $K = 3$ and $N_A = 10^3$.

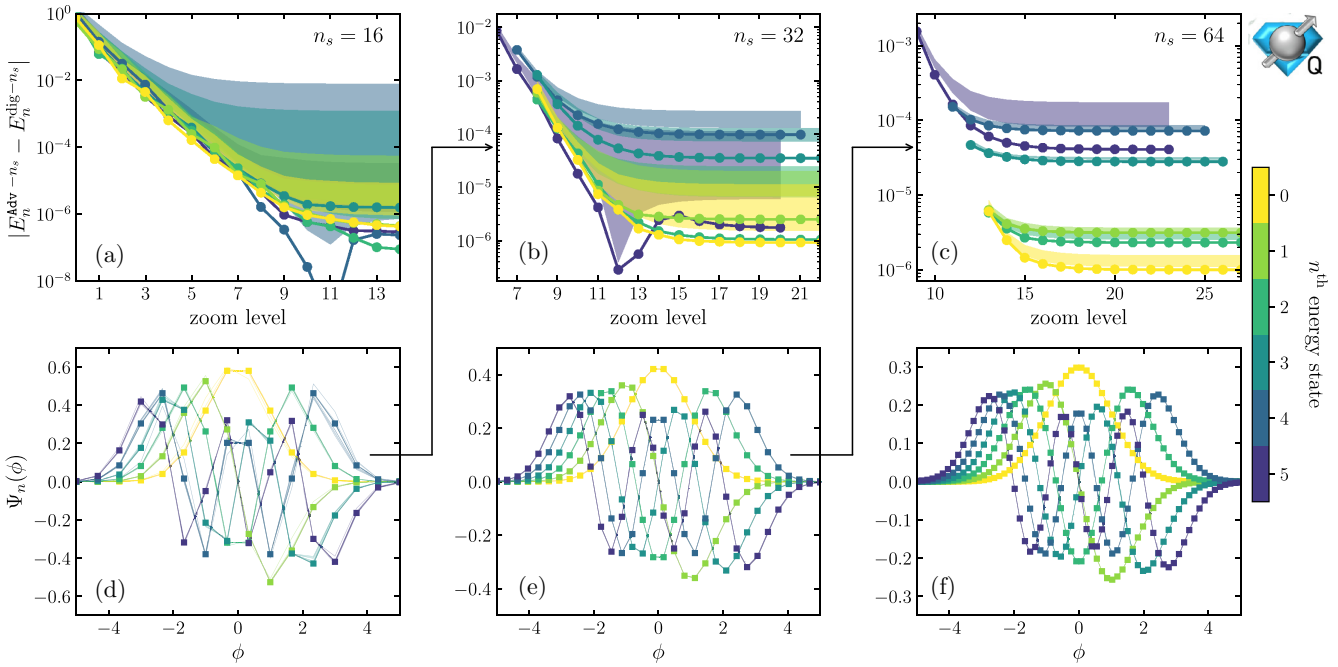

FIG. 6. (a)–(c) Convergence of the energy (in l.u.) of the first six HO states as a function of the number of zoom steps, where the solid lines with points correspond to minimum-energy solutions, while the solid bands correspond to the 68% confidence intervals determined from $N_{\mathrm{run}} = 20$ independent runs of the annealing workflow. (d)–(f) Lowest six HO wave functions [multiplied by $(-1)^n$]. The squares denote the exact values from the digitized Hamiltonian, while the lines show the $N_{\mathrm{run}} = 20$ independent runs obtained using D-Wave's Advantage with the maximal number of zoom steps. The maximum value of the field is $\phi_{\mathrm{max}} = 5$ digitized on $n_s = \{16, 32, 64\}$ states, with $K = \{3, 3, 2\}$ and $N_A = 10^3$.

$n_s = 32$ and 64 anneals, with results shown in Fig. 6 for the HO and Fig. 7 for the AHO.[3] Interestingly, while a value of $K = 3$ is sufficient for the $n_s = 16$ and 32 systems, $K = 2$ is required for the $n_s = 64$ system to permit an embedding of the QUBO matrix into Advantage.

C. Delocalized fields: $\lambda\phi^4$ with $m_0^2 < 0$ and reflection symmetry in field space

In the situation where $m_0^2 < 0$, corresponding to a double-well potential, the ground state with a symmetric wave function and the first-excited state with an antisymmetric wave function are nearly degenerate for a large region in mass-coupling space. For such parameters, the wave functions have support mainly in regions localized around the two minima of the potential, with exponential suppression of the energy difference as the minima become increasingly separated. Consequently, the results obtained with neal and Advantage are generally unable to uniquely identify the ground states of such systems. As the Hamiltonian has a reflection symmetry in field space, the near degeneracy of the lowest two states can be mitigated by solving the half space using boundary conditions at the origin consistent with a symmetric or an antisymmetric wave function. Using such implementations, the ground state and first excited state of the systems with $m_0^2 < 0$ can be uniquely determined, as shown in Fig. 8. Results are obtained with Advantage using the MG AQAE solver (with $z^{\mathrm{init}} = 3$ and using the $n_s = 16$ system as the preconditioner). It is interesting to point out that the best solution is found to have a smaller energy than one found with neal. The use of boundary conditions at the origin reduces the dimensionality of the Hamiltonian that is sent to the annealer simulator or quantum hardware, and hence the problem itself, to one similar to that of a HO with $m_0^2 > 0$. Therefore, the implementation is essentially the same as described previously. However, the delocalization of the wave function means that the digitization of the field requires an increased number of states to recover the same level of precision in, say, the ground-state energy (by maintaining a fixed δ_ϕ).

The results obtained for these systems provide practical insights into the generic performance of a QA for simulating systems with (near-)degenerate ground states. Without the half-field truncation, each converged result of the system provided, in general, a different linear combination of the (two) degenerate states, as expected. While straightforward to perform, we did not undertake a study of the m_0^2-λ parameter space to identify regions where the energy gap was sufficient for neal and Advantage to uniquely converge to the ground state.

While there is significant importance in simulating scalar fields exhibiting spontaneous symmetry breaking in 3+1 dimensions in high-energy (Higgs field) and nuclear physics (σ model and chiral perturbation theory), a detailed exploration is beyond the scope of the present work.

[3]It is interesting to note that the ground-state wave function obtained with $n_s = 16$ when interpolated to $n_s = 64$ achieves 10^{-4} precision in the ground-state energy, without using the MG-AQAE method (for higher-energy states, the precision is reduced).

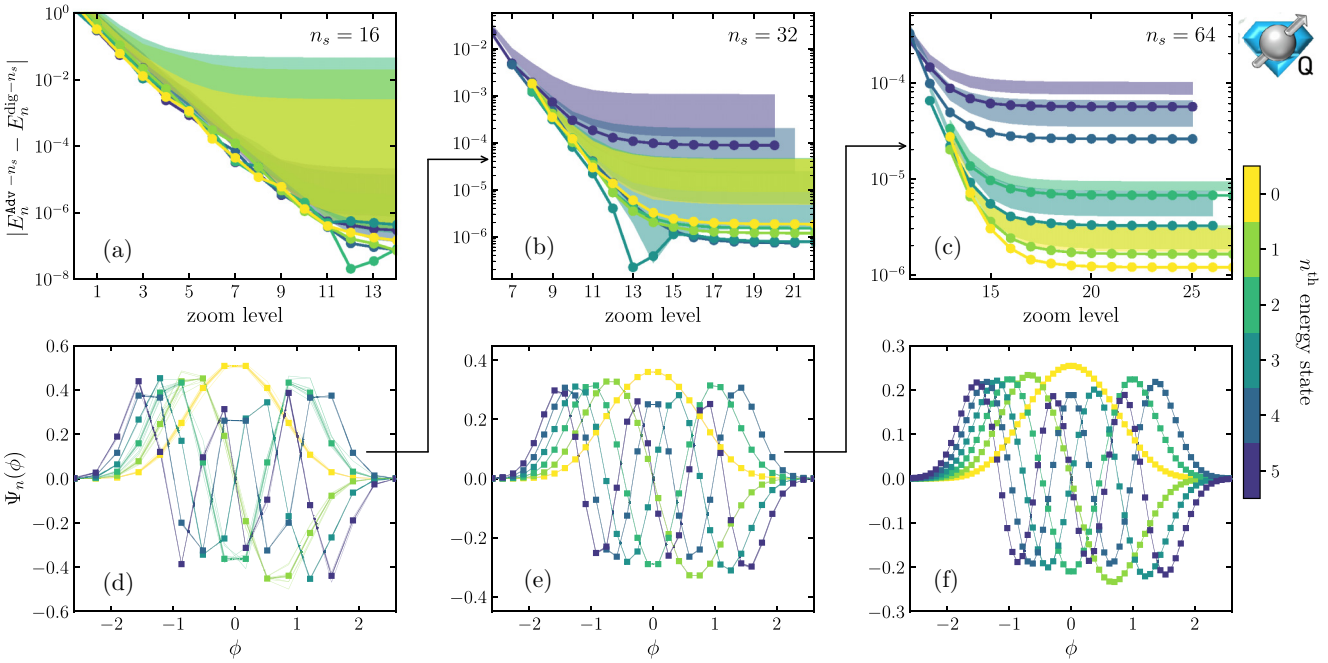

FIG. 7. (a)–(c) Convergence of the energy (in l.u.) of the first six AHO states as a function of the number of zoom steps, where the solid lines with points correspond to minimum-energy solutions, while the solid bands correspond to the 68% confidence intervals determined from $N_{\text{run}} = 20$ independent runs of the annealing workflow. (d)–(f) Lowest six AHO wave functions [multiplied by $(-1)^n$]. The squares denote the exact values from the digitized Hamiltonian, while the lines show the $N_{\text{run}} = 20$ independent runs obtained using D-Wave's Advantage with the maximal number of zoom steps. The maximum value of the field is $\phi_{\text{max}} = 2.6$ digitized on $n_s = \{16, 32, 64\}$ states, with $K = \{3, 3, 2\}$ and $N_A = 10^3$.

D. Scaling study

During this NISQ era, quantum processors are being characterized to determine their strengths and weaknesses. For this purpose, Fig. 9 shows the number of physical qubits required for the Hamiltonian in Eq. (8) with different numbers of basis states n_s. Specifically, we compute the QUBO matrix with $K = 2$ for different values of n_s, find the embedding using the `find_embedding` command from `minorminer` [88], as discussed in Sec. III B, and count the number of required physical qubits, which are shown in Fig. 9. As it uses a heuristic algorithm to find this mapping [106], the number of qubits is generally different each time this command is called, and the width of the bands represents a 68% confidence interval determined from 20 different embeddings of the same problem. Figure 9 also shows the number of qubits in the ideal case with the gray line, assuming an all-to-all connectivity, therefore requiring only Kn_s qubits.

It is interesting to note that the improvement over the previous D-Wave's QA 2000Q, with a total of 2048 qubits (and a connectivity of six qubits), to the current one, Advantage, allows for a reduction in the number of qubits by a factor of 2–3 (directly related to the increase in connectivity between qubits, which increases from 6 to 15). However, the points for both QAs follow a line with a similar slope, which is larger than the ideal case.

Although the current limit to n_s is 64, without the zooming algorithm described in Sec. II, it would be smaller (assuming the same precision on the eigenenergies), as K would have to be larger. Further, using the symmetry properties of the wave function, as in Sec. III C, the value of n_s could be doubled.

IV. REAL-TIME EVOLUTION OF PLAQUETTES AND NEUTRINOS USING FEYNMAN CLOCKS

The real-time dynamics of physically interesting complex quantum systems is an expected capability of future quantum computers, which will advance the domain of sciences beyond what is possible with classical computing. While for universal gate-based quantum computers, the challenge to implement time evolution is determining efficient quantum circuits and mappings that can be executed on available devices, the challenge for D-Wave's QAs is in finding a viable QUBO matrix that can be implemented. First formalized for scientific applications in the context of quantum chemistry [78,107], Feynman-clock states [108,109] provide a way to time evolve quantum systems in a single run of a QA (its first implementation on quantum hardware can be found in Ref. [110]). The constraint of real entries in the QUBO matrix can be circumvented by an appropriate change of basis that transforms the Hamiltonian into a purely imaginary form, rendering $\hat{U}_t = e^{-it\hat{\mathcal{H}}}$ real, for example, as used in Ref. [77]. Following the formulation of McClean *et al.* [78], called the time-embedded discrete variational principle (TEDVP), the objective function to be minimized has the form

$$F = \sum_{t,t'} \langle t'|\langle \Psi_{t'}|\hat{\mathcal{C}}|\Psi_t\rangle|t\rangle - \eta \sum_{t,t'} \langle t'|\langle \Psi_{t'}|\Psi_t\rangle|t\rangle, \qquad (12)$$

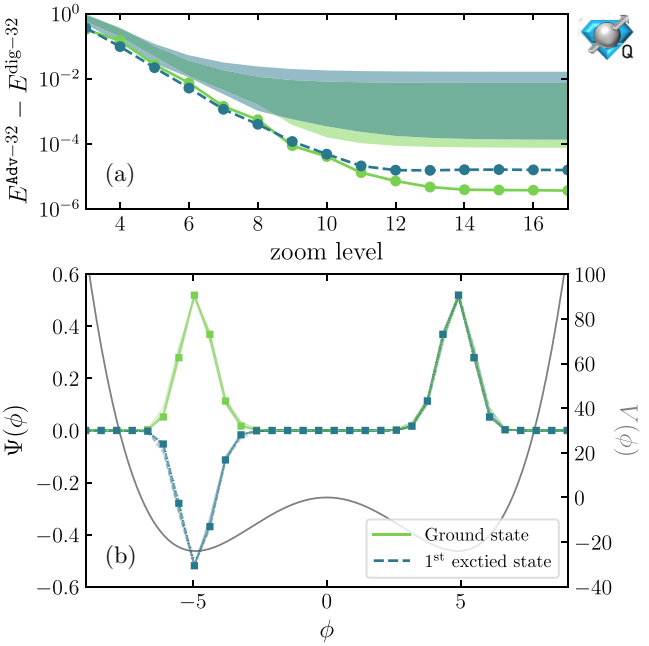

FIG. 8. Convergence of the ground-state and first-excited-state energies and wave functions of an AHO: (a) convergence of the energies (in l.u.) and (b) symmetric and antisymmetric wave functions (with the maximal number of zoom steps 17) obtained using Advantage ($N_{\text{run}} = 20$) for the system with $m_0^2 = -4$, $\lambda = 1$, and $\phi_{\max} = 9$ discretized across $n_s = 32$ states, with $K = 3$ and $N_A = 10^3$. The half-field-space Hamiltonian employed appropriate boundary conditions at the origin to independently solve for wave functions with definite reflection symmetry.

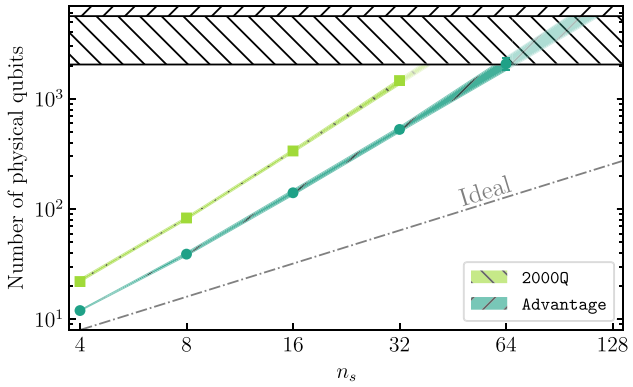

FIG. 9. Numbers of physical qubits required to map the QUBO matrix from the Hamiltonian in Eq. (8) as a function of n_s for a fixed $K = 2$. The bands show results for two available D-Wave QAs, 2000Q and Advantage, with the lighter bands being extrapolations using the last two points. The gray dot-dashed line represents the ideal scaling, with Kn_s qubits.

where the η parameter has the same purpose as in Eq. (1) and $|\Psi_t\rangle|t\rangle$ are compound states formed of the physical wave function $|\Psi_t\rangle$ and the time register $|t\rangle$. The clock Hamiltonian[4] $\hat{\mathcal{C}}$ is defined as

$$\hat{\mathcal{C}} = \hat{C}_0 + \frac{1}{2}\sum_t (\hat{I}\otimes|t\rangle\langle t| - \hat{U}_{\delta t}\otimes|t+\delta t\rangle\langle t| - \hat{U}_{\delta t}^\dagger\otimes|t\rangle\langle t+\delta t| + \hat{I}\otimes|t+\delta t\rangle\langle t+\delta t|), \tag{13}$$

with $\hat{C}_0$ a penalty term to select a particular (input) state at a time t. For our purposes, like previous works of others, we will use it to select the initial state $|\Psi_{\text{in}}\rangle$ at $t = 0$ with $\hat{C}_0 = (I - |\Psi_{\text{in}}\rangle\langle\Psi_{\text{in}}|)\otimes|0\rangle\langle 0|$. One issue that arises in using this method with a QA is that the matrix elements of $\hat{U}_{\delta t}$ are required to be computed explicitly.

We extend the formulation of the Feynman clock to allow for complex values in the QUBO elements, following Ref. [111]. In such a situation, Eq. (2) becomes

$$F^{(\mathcal{C})} = \sum_{\alpha,\beta}^{n_T\times n_s} \bar{a}_\alpha a_\beta\, \mathcal{C}_{\alpha\beta}, \tag{14}$$

where $\bar{a}_\alpha$ is the complex conjugate of a_α. Here $\mathcal{C}_{\alpha\beta}$ are matrix elements of $\hat{\mathcal{C}} - \eta\hat{I}$ between basis states spanning $|\Psi_t\rangle|t\rangle$, of which there are $n_T \times n_s$, where n_T is the number of time slices and n_s is the number of basis states of the Hamiltonian. Since $\hat{\mathcal{C}}$ is Hermitian, terms in Eq. (14) can be written as, after the summations,

$$\bar{a}_\alpha a_\beta \mathcal{C}_{\alpha\beta} = a_\alpha^{\text{Re}} a_\beta^{\text{Re}} \mathcal{C}_{\alpha\beta}^{\text{Re}} - a_\alpha^{\text{Re}} a_\beta^{\text{Im}} \mathcal{C}_{\alpha\beta}^{\text{Im}} + a_\alpha^{\text{Im}} a_\beta^{\text{Re}} \mathcal{C}_{\alpha\beta}^{\text{Im}} + a_\alpha^{\text{Im}} a_\beta^{\text{Im}} \mathcal{C}_{\alpha\beta}^{\text{Re}}, \tag{15}$$

which involves only real numbers. With this form, together with Eq. (5) for the fixed-point representation of the real and imaginary parts of a_α, the elements of the QUBO matrix, $Q_{\alpha,i;\beta,j}$, become

$$Q_{\alpha,i;\beta,j} = \begin{cases} 2^{i+j-2K-2z}(-1)^{\delta_{iK}+\delta_{jK}}\mathcal{C}_{\alpha\beta}^{\text{Re}} + 2\delta_{\alpha\beta}\delta_{ij}2^{i-K-z}(-1)^{\delta_{iK}}\sum_\gamma\left(a_\gamma^{\text{Re},(z)}\mathcal{C}_{\gamma\beta}^{\text{Re}} + a_\gamma^{\text{Im},(z)}\mathcal{C}_{\gamma\beta}^{\text{Im}}\right), & 1\leqslant i,j\leqslant K \\ -2^{i+j'-2K-2z}(-1)^{\delta_{iK}+\delta_{j'K}}\mathcal{C}_{\alpha\beta}^{\text{Im}}, & 1\leqslant i,j'\leqslant K \\ 2^{i'+j-2K-2z}(-1)^{\delta_{i'K}+\delta_{jK}}\mathcal{C}_{\alpha\beta}^{\text{Im}}, & 1\leqslant i',j\leqslant K \\ 2^{i'+j'-2K-2z}(-1)^{\delta_{i'K}+\delta_{j'K}}\mathcal{C}_{\alpha\beta}^{\text{Re}} + 2\delta_{\alpha\beta}\delta_{i'j'}2^{i'-K-z}(-1)^{\delta_{i'K}}\sum_\gamma\left(a_\gamma^{\text{Im},(z)}\mathcal{C}_{\gamma\beta}^{\text{Re}} - a_\gamma^{\text{Re},(z)}\mathcal{C}_{\gamma\beta}^{\text{Im}}\right), & 1\leqslant i',j'\leqslant K, \end{cases} \tag{16}$$

where, to accommodate both real and imaginary parts of a_α, the index i resides in the range $1 \leqslant i \leqslant 2K$, with $1 \leqslant i \leqslant K$ for a_α^{Re} and $(K+1) \leqslant i \leqslant 2K$ for a_α^{Im}, with $i' \equiv i - K$ (the derivation of this expression can be found in Appendix A). The dimension of the QUBO matrix using n_T time slices with the TEDVP formalism is $2Kn_Tn_s \times 2Kn_Tn_s$ [a factor of $(2n_T)^2$ times larger than that used to determine wave functions of the Hamiltonian, as described in Sec. II].

[4]This is constructed in the context of superpositions of time slices via projectors formed from $|t\rangle_- = \frac{1}{\sqrt{2}}(|t\rangle - |t+\delta t\rangle)$.

In the following sections we examine two systems of physical interest to standard-model research, the time evolution of a single plaquette of SU(3) Yang-Mills lattice gauge theory and of a four-neutrino system, using Advantage. Both of these systems have been simulated previously using IBM's superconducting quantum computers, with two and four qubits. In studying these systems with Advantage, the following values of parameters were found to be effective: $N_A = 10^3$, $N_{\rm run} = 20$, $K = 2$, $\eta = 0$, and $\{z^{\rm init}, z^{\rm max}\} = \{0, 14\}$. The chain strength coefficient is fixed to $\omega = 0.2$ and the default annealing-schedule parameters ($t_A = 20\ \mu$s) are used.

A. One plaquette in SU(3) Yang-Mills lattice gauge theory

Quantum simulations of non-Abelian lattice gauge theories are anticipated to become increasingly important in standard-model research. Progress toward this objective is at its earliest stages, with simulations of small systems in low dimensions underway using the available NISQ-era devices, e.g., Refs. [[10,77,80,112–151]]. The Kogut-Susskind Hamiltonian [152,153] provides one concrete framework for quantum simulations of lattice gauge theories and is being actively pursued with superconducting devices, trapped ion systems, optical systems, superconducting radio-frequency cavities, and QAs. Simulations of small systems have been performed in one and two spatial dimensions, with simulations of the smallest three-dimensional systems barely within reach of today's devices. Extensive efforts are underway to develop techniques to make simulations with this framework more practical, for instance, integrating over the gauge spaces at each lattice site [131,137]. Other mappings of the gauge fields, for instance, quantum link models (e.g., Refs. [154–157]), spin systems, and the discrete sampling of gauge fields (e.g., Refs. [158,159]) are under active exploration. While the formal construction for quantum simulations of non-Abelian gauge theories has been established for more than a decade and concrete protocols for implementation on quantum devices known for a comparable period of time, first implementations appeared in 2016 using trapped-ion systems [125] and soon after using superconducting [132] and optical systems [134]. More recently, the first simulations of SU(3) Yang-Mills theories were performed [80] of one and two plaquettes, building upon previous simulations of SU(2) plaquette systems [137] and one-dimensional SU(2) chains [146]. These small systems can be simulated using D-Wave's annealers, as was first demonstrated for the SU(2) plaquette systems in the work of A Rahman *et al.* [77].

The time evolution of one and two plaquettes in SU(3) Yang-Mills gauge theory has been simulated using IBM's Athens quantum computer [80]. Both a local basis and global bases were simulated, with the single plaquette a particularly simple system with a minimal qubit footprint in the global basis due to Gauss's law restrictions. In this work we focus on a one-plaquette system in the color parity basis, including the states $\{|\mathbf{1}\rangle, |\mathbf{3}^+\rangle, |\mathbf{6}^+\rangle, |\mathbf{8}\rangle\}$, which has the following Hamiltonian when mapped to two qubits:

$$\hat{\mathcal{H}} = g^2\left(\frac{23}{6}\hat{I}\otimes\hat{I} - \frac{5}{2}\hat{Z}\otimes\hat{I} - \frac{1}{2}\hat{I}\otimes\hat{Z} - \frac{5}{6}\hat{Z}\otimes\hat{Z}\right) - \frac{1}{2g^2}\left[\sqrt{2}\hat{I}\otimes\hat{X} + \sqrt{2}\hat{X}\otimes\left(\frac{\hat{I}-\hat{Z}}{2}\right) + \frac{1}{2}\hat{X}\otimes\hat{X} + \frac{1}{2}\hat{Y}\otimes\hat{Y} + \frac{1}{4}(\hat{I}+\hat{Z})\otimes(\hat{I}-\hat{Z}) - 6\,\hat{I}\otimes\hat{I}\right]. \quad (17)$$

Here $\hat{X}$, $\hat{Y}$, and $\hat{Z}$ are the Pauli matrices. The utility of color parity arises from the Hamiltonian containing only the symmetric combination of the plaquette operator $\square + \square^\dagger$ and the trivial vacuum being even under color parity transformation. Simulations performed with IBM's Athens used a strong coupling constant of $g = 1$. The system was time evolved using a Trotterized decomposition of the evolution operator to enable an efficient mapping onto quantum circuits [80]. Both first- and second-order Trotterizations were employed, using a single step ($\delta t = t$) and multiple steps ($\delta t = t/2$) for both. Applying standard error mitigation techniques [for controlled-NOT (CNOT) errors] and fitting systematic error estimation, the vacuum-to-vacuum probability $|\langle\mathbf{1}|\hat{U}_t|\mathbf{1}\rangle|^2$ (the vacuum is the plaquette in the $|\mathbf{1}\rangle \equiv |0\rangle\otimes|0\rangle$ state) and the expectation value of the electric energy [the g^2 terms in Eq. (17)] were computed as a function of time, as shown in Fig. 8 of Ref. [80].

In the present work, using exact matrix exponentiation of the Hamiltonian to determine the evolution operator over the time interval δt, a QUBO matrix describing the Feynman-clock evolution of this system was formed. Using the techniques described in previous sections to find eigenstates and energies, Advantage was used to evolve the SU(3) plaquette system forward in time from an initial state of the trivial vacuum. Results obtained for the vacuum-to-vacuum persistent probability and for the energy in the electric field using Advantage are shown in Fig. 10. These results are found to agree with exact theoretical curves within uncertainties. Further, the precision of the results is significantly better than that obtained previously using IBM's Athens [80].

B. Neutrino flavor dynamics in beam-beam collisions

Neutrino flavor dynamics is a major focus of research in standard-model physics. While neutrinos are rendered massless by dimension-4 operators in the standard model, a result of the local gauge symmetries and particle content, in particular the absence of a right-handed neutrino field, the unambiguous observations of neutrino flavor dynamics, and nonzero mass differences, provides unique insight into aspects of physics beyond the standard model and the structure of higher-dimension operators. The connection between lepton-number violating Majorana neutrino masses and interactions that induce neutrinoless $\beta\beta$ decay of nuclei is a strong theoretical motivation driving the current experimental program(s) searching for such processes (for a recent review, see, e.g., Ref. [160]). Nonzero neutrino masses, when combined with standard-model electroweak interactions, have implications for matter under the extreme conditions of density and temperature that are found in the early universe (see, e.g., Refs. [161–163]) and core-collapse supernova (see, e.g., Refs. [162,164]) (for recent works, see, e.g., Ref. [165]). Decades of work on this subject continue to uncover new phenomena in neutrino dynamics in these environments, including the recent identification of dynamical phase

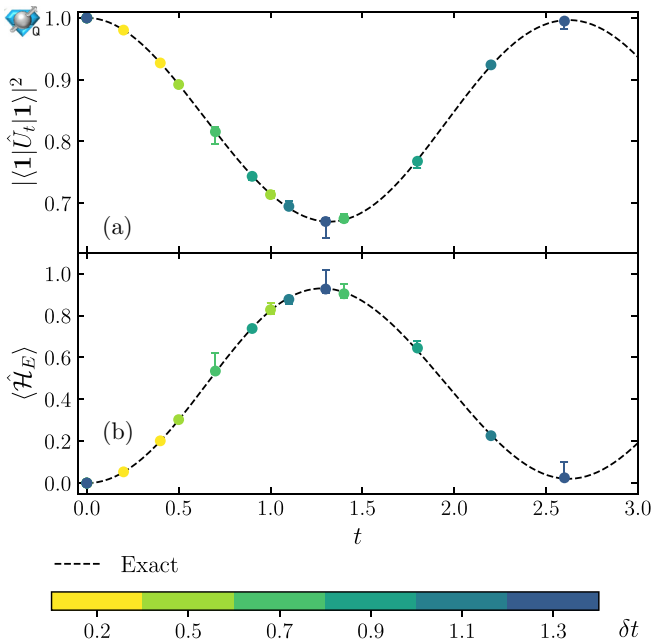

FIG. 10. (a) Vacuum-to-vacuum probability $|\langle \mathbf{1}|\hat{U}_t|\mathbf{1}\rangle|^2$ and (b) energy (in units of g^2) in the electric field of the one-plaquette system as a function of time (in units of $1/g^2$). The circles correspond to results obtained using D-Wave's QA Advantage with the maximal number of zoom steps ($z^{\max} = 14$), $K = 2$, $N_A = 10^3$ anneals, different time shifts δt, and $n_T = 3$ time steps $\{0, \delta t, 2\delta t\}$. The uncertainties correspond to the 68% confidence intervals determined from $N_{\text{run}} = 20$ independent runs. The dashed curves correspond to the exact theoretical curves.

transitions in collective dynamics and correlations with quantum entanglement [166–174]. With their importance in transport from within the core, high-precision simulations of the evolution of supernova require the inclusion of three-dimensional neutrino distributions with detailed quantum kinetics, a problem that has been estimated to lie beyond classical exascale computing. This has prompted the increasing number of explorations of neutrino dynamics using quantum simulations [81,175,176] and modern theoretical tools using entanglement as an essential ingredient, e.g., tensor networks [173,174,177], and with, for example, classical simulations utilizing symmetries and matrix sparsity [178] to study systems currently beyond the reach of matrix product states. These works constitute important explorations of the roles of quantum information, entanglement, and real-time dynamics in dense neutrino systems and make inroads into unifying previously identified collective phenomena while searching for new behaviors.

One such recent detailed study, which we parallel, by Hall *et al.* [81], performed quantum simulations of systems of $N = 4$ neutrinos, restricted to two active flavors and without the inclusion of electroweak interactions with matter (such as $e^{\pm}$, $\mu^{\pm}$, and $q, \overline{q}$) but with self-interactions. Using the known mapping of the two-flavor neutrino system to quantum spin models, it was simulated using IBM's Vigo superconducting quantum computer for a selection of parameters, including mass differences and neutrino densities, using the effective Hamiltonian,

$$\hat{\mathcal{H}} = \frac{1}{2}\sum_i^N \left(-\Delta_i \cos 2\theta_v \sigma_i^z + \Delta_i \sin 2\theta_v \sigma_i^x\right) + \kappa \sum_{i<j}^N (1 - \cos\theta_{ij})\boldsymbol{\sigma}_i \cdot \boldsymbol{\sigma}_j, \tag{18}$$

where θ_v is the flavor mixing angle (which is set to $\theta_v = 0.195$ for this model) and $\Delta_i = \delta m^2/2E_i$ is the strength of the one-body term determined by the difference in neutrino squared masses δm^2 and the energy of each neutrino E_i. The strength of the two-body term κ depends on the neutrino density and electroweak couplings and θ_{ij} is the angle between the momenta of the ith and jth neutrinos. The spin operators $\boldsymbol{\sigma}_i$ act in the two-dimensional neutrino flavor space $\boldsymbol{\nu}_i = (\nu_{i,e}, \nu_{i,\mu})^T$.

For the test-case model simulation presented in Ref. [81], a monochromatic neutrino beam is assumed, with $E_i = \delta m^2/4\kappa$ and with an anisotropic distribution of momentum directions $\theta_{ij} = \arccos(\zeta)|i - j|/(N - 1)$, with $\zeta = 0.9$, i.e., $\theta_{12} = \theta_{23} = \theta_{34} = \frac{1}{3}\arccos(\zeta)$, $\theta_{13} = \theta_{24} = \frac{2}{3}\arccos(\zeta)$, and $\theta_{14} = \arccos(\zeta)$. The time evolution of the system was determined by first-order Trotterization of the evolution operator derived from the Hamiltonian separated into neutrino-pair terms (as opposed to one- and two-body operators) [81]. One of the observables examined was the probability of the ith neutrino transforming between flavors $\nu_e \leftrightarrow \nu_\mu$,

$$P_i(t) = \tfrac{1}{2}\langle \Psi_t|1 \mp \sigma_i^z|\Psi_t\rangle, \tag{19}$$

starting with $|\Psi_0\rangle = |\nu_e\nu_e\nu_\mu\nu_\mu\rangle$ and with the sign depending on the initial state of the system $\nu_{i,e}$ $(-)$ or $\nu_{i,\mu}$ $(+)$. The results of those simulations can be found in Figs. 3 and 4 of their paper [81]. The evolution of flavor entanglement in the four-neutrino system was also studied in Ref. [81]. The single-neutrino entanglement entropy is given by

$$S_i(t) = -\text{Tr}\{\rho_i(t)\log_2[\rho_i(t)]\}, \tag{20}$$

where $\rho_i(t)$ is the reduced density matrix for the ith neutrino, with $\rho_i(t) = \text{Tr}_{j\neq i}[|\Psi_t\rangle\langle\Psi_t|]$. The concurrence was also studied [81], and in this work we consider the logarithmic negativity

$$\mathcal{N}_{ij}(t) = \log_2 \|\rho_{ij}^{\Gamma}(t)\|_1, \tag{21}$$

where $\rho_{ij}(t)$ is the two-neutrino reduced density matrix for the ij neutrino pair, Γ indicates the partial transposition of ρ, and $\|\cdot\|_1$ is the trace norm. The logarithmic negativity, related to the concurrence, is an upper bound on the distillable entanglement. The neutrino Hamiltonian in Eq. (18) is invariant under neutrino exchanges $1 \leftrightarrow 4$ and $2 \leftrightarrow 3$ [81]. This gives rise to relations between observables, such as $P_1(t) = P_4(t)$, $S_1(t) = S_4(t)$, and $\mathcal{N}_{12}(t) = \mathcal{N}_{34}(t)$.

The results of our quantum simulations obtained using Advantage are shown in Figs. 11 and 12. The implementation of the clock state using the matrix representation of the exact evolution operator between time slices, without Trotterization into products of unitaries associated with neutrino pairs, eliminates a significant source of ("theory") systematic error imposed by circuit-volume limitations of available devices with different architectures, as can be seen by comparing the

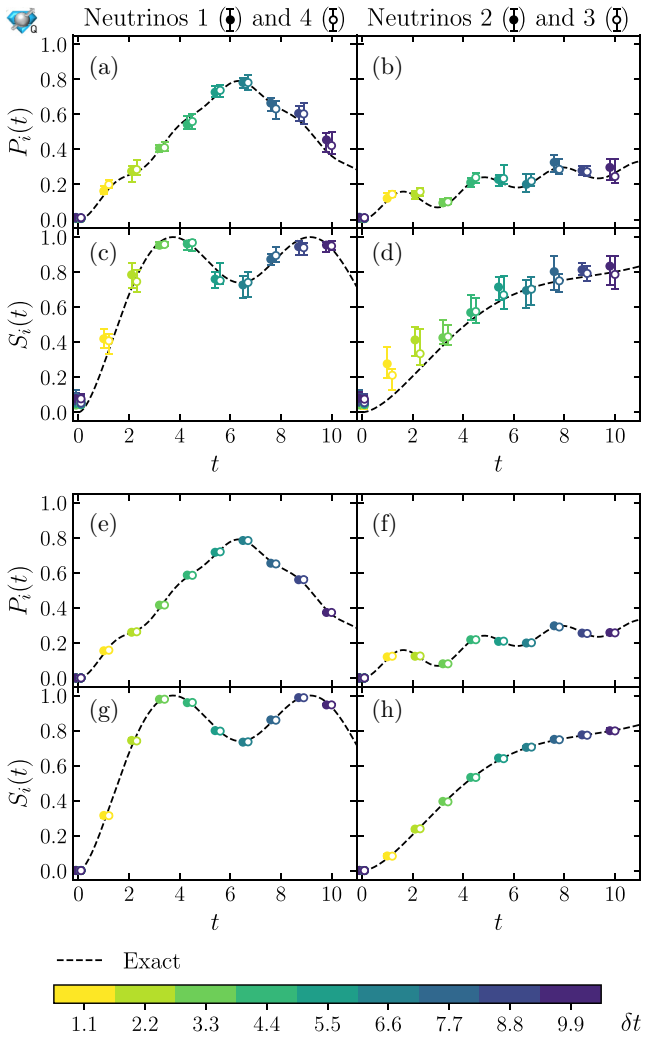

FIG. 11. (a), (b), (e), and (f) Probability of flavor transitions and (c), (d), (g), and (h) single-neutrino entanglement entropy for the (a), (c), (e), and (g) first and fourth and (b), (d), (f), and (h) second and third neutrinos as a function of time (in units of $1/\kappa$). The results are obtained using D-Wave's QA Advantage with the maximal number of zoom steps, $K = 2$, $N_A = 10^3$ anneals, different time shifts δt, and $n_T = 2$ time steps $\{0, \delta t\}$ (they have been shifted slightly along the x axis for clarity). (a)–(d) show the raw results, while (e)–(h) show the results after two iterations of the procedure described in the text. The uncertainties correspond to the 68% confidence intervals determined from $N_{\text{run}} = 20$ independent runs. The dashed curves correspond to the exact theoretical curves.

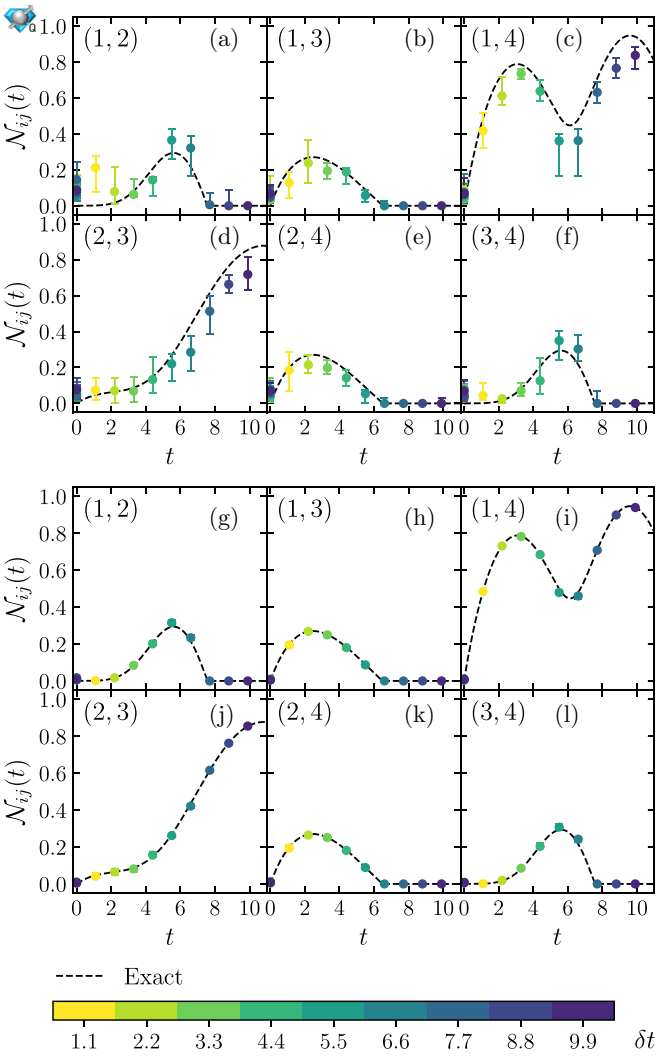

FIG. 12. Logarithmic negativity of pairs of neutrinos as a function of time (in units of $1/\kappa$). The results are obtained using D-Wave's QA Advantage with the maximal number of zoom steps, $K = 2$, $N_A = 10^3$ anneals, different time shifts δt, and $n_T = 2$ time steps $\{0, \delta t\}$. (a)–(f) show the raw results, while (g)–(l) show the results after two iterations of the procedure described in the text. The uncertainties correspond to 68% confidence intervals determined from $N_{\text{run}} = 20$ independent runs. The dashed curves correspond to the exact theoretical curves.

results shown in Figs. 11 and 12 and the results presented in Figs. 3, 4, and 6 of Ref. [81]. Further, and equally important, the absence of systematic errors associated with device performance in the simulation, dominated by CNOT gates and subsequent mitigation procedures, improves the accuracy of the simulations of this system that are possible with Advantage compared with other quantum devices.

The uncertainties associated with the dynamics of four neutrinos are considerably larger than for those associated with the single plaquette of SU(3) Yang-Mills lattice gauge theory, discussed in the preceding section. This is due to a larger QUBO matrix that is passed to the annealer and is one indication of the scaling of the capabilities of Advantage with increasing system size. Adding one more neutrino to the system renders the problem intractable for Advantage as the QUBO matrix will not fit onto its QPU.[5] Additionally, it can be seen that the uncertainties for the logarithmic negativity in Fig. 12 are larger than those of the single-neutrino entanglement entropy in Fig. 11, which are in turn larger than

[5]We attempted to study the $N = 5$ neutrino system with Advantage by setting $K = 1$, but the results (and uncertainty estimations) obtained were unreliable. One of the issues is that a_α, with $K = 1$, only takes two values $\{-1, 0\}$, requiring a large value of η to prevent the null solution.

the neutrino flavor transition probability, also in Fig. 11. The study of such quantum correlations requires high-precision calculations. In some cases, the wave functions $|\Psi_t\rangle$ are determined with 10^{-1}–10^{-2} precision, which is seen to be insufficient.

One way of improving the results (and reduce uncertainties) is to increase the number of anneals N_A by a factor ξ. As this leads to only a $1/\sqrt{\xi}$ reduction in the uncertainty in energies, this (brute force) approach demands excessive computational resources. A better method for reducing the uncertainties is analogous to the multigrid method used in Sec. III. The challenge here is that it is not straightforward to define the Hamiltonian for a smaller system to provide interpolating wave functions for the larger system [the four-neutrino case is not continuously connected to the two- and three- (or five-)neutrino systems]. We have found that using the solution from the QA as a starting point for a subsequent anneal, but with $z \neq 0$ (to narrow the window of a_α that the QA can explore), leads to approximately a one-order-of-magnitude reduction in the uncertainty in the energy (while only doubling the number of anneals). As an example, the results obtained after two steps of this iterative procedure are shown (in panels below the raw results) in Figs. 11 and 12 and show clear reductions in the uncertainties.

This iterative procedure can be repeated several times until no further improvement is obtained. For the four-neutrino system, we obtain an ultimate precision of 10^{-16} in the energy and 10^{-8}–10^{-10} in the flavor transition probability, single-neutrino entanglement, and logarithmic negativity (as shown in Fig. 13 for $t = 1.1$, in units of $1/\kappa$). It appears that the success of this iterative method is due in part to the ground-state energy of the TEDVP objective function being *a priori* known to vanish.

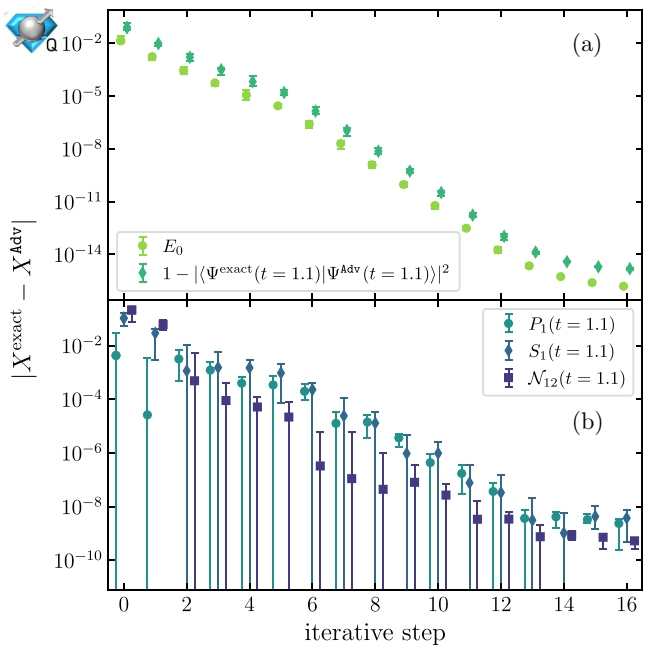

FIG. 13. (a) Convergence of the ground-state energy and wave function and (b) flavor transition probability, single-neutrino entanglement, and logarithmic negativity as a function of the number of steps of the iterative procedure described in the text. The results are obtained using D-Wave's QA Advantage with the maximal number of zoom steps, $K = 2$, and $N_A = 10^3$ anneals. The uncertainties correspond to 68% confidence intervals determined from $N_{\rm run} = 20$ independent runs.

In contrast to the calculations with IBM's superconducting hardware, where scaling to larger problems is limited by qubit and gate fidelity, along with connectivity, for increasing qubit requirements, the qubit footprint on the annealing devices naively scales exponentially with the number of neutrinos. This is expected to be mitigated using techniques that have enabled classical computing to provide a series of precision calculations in these model systems.

V. CONCLUSION

We have explored the potential of D-Wave's quantum annealers for simulating some key basic aspects of standard-model physics. In particular, the eigenstates and energies of the lowest-lying states of the harmonic oscillator and anharmonic oscillator were studied using zooming and a basic coordinate-space multigrid (MG AQAE). Deviations in the extracted energies were less than approximately 10^{-4}. These simulations are the basic elements of lattice scalar field theory of importance, for instance, low-energy chiral nuclear physics or high-energy Higgs physics. The time evolution of a single plaquette of SU(3) Yang-Mills gauge theory truncated to $\{|\mathbf{1}\rangle, |\mathbf{3}^+\rangle, |\mathbf{6}^+\rangle, |\mathbf{8}\rangle\}$ in the color parity basis and of neutrino flavor in a monochromatic beam with angular dispersion were also studied through a refinement of the Feynman-clock algorithm, with deviations that can be reduced below 10^{-8}. The results of our quantum simulations of the plaquette and neutrino evolution were found to compare favorably with previous quantum simulations performed using IBM's superconducting quantum computers.

Except for the cases in which the Hamiltonian of interest directly maps (or can be efficiently transformed) onto the annealer, which is optimal for transverse-field Ising models (e.g., Ref. [45]), with the current formulation, the qubit requirements on the device scale with size of the Hilbert space. Therefore, the maximum dimensionality of the systems that we have considered in this work that can be addressed with Advantage remains small. For the harmonic and anharmonic oscillators, the maximum number of states in the decimation of the field wave function that we could reliably simulate was $n_s = 64$. For time evolution, due to the extra $2n_T$ factor in the dimensions of the QUBO matrix, this decimation is reduced to 16. Further, there is a somewhat unfortunate dependence on the η parameter, although this can be partially mitigated by performing a more structured scan, as shown in Ref. [56]. It seems that paths forward for simulating quantum field theories require efficiently utilizing the innate Ising-Hamiltonian architectures of the annealers, including the dynamics of the annealing process. A step in this direction has been taken in Refs. [179,180], which utilize the JLP field mapping to qubits but not the quantum Fourier transform onto conjugate momentum space, and has the potential to improve the scaling of ground-state preparation. With the current formulation, the main application can be the preparation of states which are later used in universal quantum computers to perform time evolution, acting as preconditioners to speed up the process of

TABLE III. Comparison of the (average) time (in seconds) taken to perform $N_A = 10^3$ anneals for a specific problem size (fixed n_s and K) and for a single zoom step between the simulator neal, run on a 2.40-GHz Intel Core i9-9980HK CPU, and the quantum processor Advantage ($t_A = 20\ \mu$s), with and without including the time for the embedding.

Problem size	neal (s)	Advantage (without embedding) (s)	Advantage (with embedding) (s)
$n_s = 16, K = 3$	0.7	0.15	10.15
$n_s = 32, K = 3$	2.0	0.20	100.20
$n_s = 64, K = 2$	2.6	0.25	200.25

finding ground states using domain decomposition techniques to reduce the size of the problem (for example, by computing the angles to set up the wave function for a scalar field theory [181]). A somewhat different implementation employing Floquet engineering also has promise [182].

ACKNOWLEDGMENTS

This work was supported in part by the U.S. Department of Energy, Office of Science, Office of Nuclear Physics, InQubator for Quantum Simulation under Award No. DOE (NP) DE-SC0020970 (M.J.S.) and the Quantum Science Center, a National Quantum Information Science Research Center of the U.S. Department of Energy (M.I.). All calculations performed on D-Wave's QAs were through cloud access [105]. We made extensive use of Wolfram *Mathematica* [101], PYTHON [99,183], and JUPYTER notebooks [100] in the CONDA environment [184]. This work was enabled in part by the use of advanced computational, storage, and networking infrastructure provided by the Hyak supercomputer system at the University of Washington.

APPENDIX A: THE QUBO MATRIX

In this Appendix, an outline is presented of the derivation of expressions for the QUBO matrix used in Sec. II to compute eigenstates and energies of a given Hamiltonian and in Sec. IV to determine the timeevolution of an SU(3) Yang-Mills plaquette and a system of four neutrinos.

Starting from the objective function in Eq. (2) for the eigenstates and energies of a given Hamiltonian and using the fixed-point representation for the zoom coefficients in Eq. (5),

$$F = \sum_{\alpha\beta} a_\alpha a_\beta h_{\alpha\beta} = \sum_{\alpha\beta}\left[a_\alpha^{(z)} + \sum_i 2^{i-K-z}(-1)^{\delta_{iK}} q_i^\alpha\right] \times \left[a_\beta^{(z)} + \sum_j 2^{j-K-z}(-1)^{\delta_{jK}} q_j^\beta\right] h_{\alpha\beta}, \tag{A1}$$

which consists of three different types of terms. The first type is the product of $a_\alpha^{(z)} a_\beta^{(z)}$, without q_i^α variables. It provides a constant offset to F, which does not modify the position of the minimum and thus can be omitted from the QUBO matrix. The second type comes from the product of terms with q_i^α and q_j^β, which is of the desired form in Eq. (4), and multiplied with a 2^{-2z} zooming factor. The last type originates from the product of $a_\alpha^{(z)}$ with q_j^β, which, as it involves a single q_j^β, naively has the potential to be problematic for forming a viable QUBO matrix. The difficulty is averted by using a defining property of binary variables, $q_j^\beta = (q_j^\beta)^2$, leading to, for example,

$$\begin{aligned}
&\sum_{\alpha\beta} a_\alpha^{(z)} \sum_j (-1)^{\delta_{jK}} 2^{j-K-z} q_j^\beta h_{\alpha\beta} \\
&= \sum_{\beta,j} (-1)^{\delta_{jK}} 2^{j-K-z} q_j^\beta q_j^\beta \underbrace{\left(\sum_\alpha a_\alpha^{(z)} h_{\alpha\beta}\right)}_{\alpha\to\gamma} \\
&= \sum_{\alpha\beta,ij} \delta_{\alpha\beta}\delta_{ij} (-1)^{\delta_{jK}} 2^{j-K-z} q_i^\alpha q_j^\beta \sum_\gamma a_\gamma^{(z)} h_{\gamma\beta}.
\end{aligned} \tag{A2}$$

TABLE V. Differences between the digitized energies and the corresponding results obtained using D-Wave's Advantage for the AHO with $m_0^2 = -4$, $\lambda = 1$, and $\phi_{\max} = 9$, shown in Fig. 8, with $n_s = 32, K = 3, N_A = 10^3$, and the maximum number of zoom steps. The uncertainties correspond to 68% confidence intervals determined from $N_{\text{run}} = 20$ independent runs.

n	$\lvert\delta E_n^{\text{Adv}-32}\rvert$
0	$(2.5^{+5.0}_{-2.4}) \times 10^{-3}$
1	$(1.2^{+16}_{-1.1}) \times 10^{-3}$

TABLE IV. Differences between the digitized energies and the corresponding results obtained using D-Wave's Advantage for the HO with $m_0 = 1$ and $\phi_{\max} = 5$ and the AHO with $m_0 = 1$, $\lambda = 32$, and $\phi_{\max} = 2.6$, shown in Figs. 6 and 7, with $n_s = \{16, 32, 64\}$, $K = \{3, 3, 2\}$, $N_A = 10^3$, and the maximum number of zoom steps. The uncertainties correspond to 68% confidence intervals determined from $N_{\text{run}} = 20$ independent runs.

n	$\lvert\delta E_n^{\text{Adv}-16}\rvert_{\text{HO}}$	$\lvert\delta E_n^{\text{Adv}-32}\rvert_{\text{HO}}$	$\lvert\delta E_n^{\text{Adv}-64}\rvert_{\text{HO}}$	$\lvert\delta E_n^{\text{Adv}-16}\rvert_{\text{AHO}}$	$\lvert\delta E_n^{\text{Adv}-32}\rvert_{\text{AHO}}$	$\lvert\delta E_n^{\text{Adv}-64}\rvert_{\text{AHO}}$
0	$(2.4^{+6.1}_{-1.5}) \times 10^{-6}$	$(3.9^{+7.8}_{-2.3}) \times 10^{-6}$	$(1.2^{+0.3}_{-0.1}) \times 10^{-6}$	$(3.4^{+22}_{-3.4}) \times 10^{-4}$	$(1.5^{+3.0}_{-1.0}) \times 10^{-5}$	$(1.9^{+1.1}_{-0.2}) \times 10^{-6}$
1	$(3.6^{+52}_{-1.9}) \times 10^{-6}$	$(9.6^{+11}_{-2.6}) \times 10^{-6}$	$(3.6^{+0.2}_{-0.2}) \times 10^{-6}$	$(2.6^{+186}_{-2.6}) \times 10^{-4}$	$(1.9^{+2.4}_{-1.1}) \times 10^{-5}$	$(2.7^{+0.5}_{-0.9}) \times 10^{-6}$
2	$(1.9^{+5.5}_{-1.2}) \times 10^{-6}$	$(9.8^{+15}_{-3.1}) \times 10^{-6}$	$(2.8^{+0.4}_{-0.2}) \times 10^{-6}$	$(0.7^{+4487}_{-0.7}) \times 10^{-5}$	$(2.2^{+2.4}_{-1.7}) \times 10^{-5}$	$(8.3^{+1.0}_{-0.9}) \times 10^{-6}$
3	$(0.8^{+117}_{-0.6}) \times 10^{-5}$	$(9.7^{+1.5}_{-0.3}) \times 10^{-5}$	$(30^{+1.8}_{-0.2}) \times 10^{-6}$	$(1.7^{+1.8}_{-0.9}) \times 10^{-6}$	$(0.7^{+1.8}_{-0.8}) \times 10^{-5}$	$(6.0^{+1.4}_{-2.0}) \times 10^{-6}$
4	$(0.5^{+744}_{-0.5}) \times 10^{-5}$	$(1.6^{+1.1}_{-0.3}) \times 10^{-4}$	$(8.0^{+0.6}_{-0.7}) \times 10^{-5}$	$(0.6^{+14}_{-0.5}) \times 10^{-6}$	$(6.3^{+14}_{-4.1}) \times 10^{-5}$	$(5.3^{+1.1}_{-1.8}) \times 10^{-5}$
5	$(2.9^{+29}_{-1.8}) \times 10^{-6}$	$(4.7^{+6.6}_{-5.3}) \times 10^{-5}$	$(1.3^{+0.5}_{-0.5}) \times 10^{-4}$	$(1.5^{+20}_{-0.7}) \times 10^{-6}$	$(6.1^{+4.2}_{-4.9}) \times 10^{-4}$	$(8.1^{+1.9}_{-0.6}) \times 10^{-5}$

TABLE VI. Number of physical qubits required to map the QUBO matrix for the two available D-Wave's QAs, shown in Fig. 9, with $K = 2$. The uncertainties correspond to 68% confidence intervals determined from 20 different embedding with the same problem.

n_s	2000Q	Advantage
4	22^{+1}_{-0}	12^{+0}_{-0}
8	83^{+1}_{-2}	39^{+1}_{-1}
16	337^{+8}_{-9}	141^{+8}_{-6}
32	1464^{+39}_{-109}	528^{+24}_{-26}
64		2077^{+293}_{-254}

As $h_{\alpha\beta}$ is symmetric, the two contributions of this form give the same contribution, leading to a QUBO matrix of the form, as given in Eq. (6),

$$Q_{\alpha,i;\beta,j} = 2^{i+j-2K-2z}(-1)^{\delta_{iK}+\delta_{jK}}h_{\alpha\beta} + 2\delta_{\alpha\beta}\delta_{ij}2^{i-K-z}(-1)^{\delta_{iK}}\sum_{\gamma}a_{\gamma}^{(z)}h_{\gamma\beta}. \quad \text{(A3)}$$

In order to reduce this four-index array into a more manageable matrix form, following Ref. [77], the indices α and i are combined into $n = K(\alpha-1)+i$.

To construct the QUBO matrix for time evolution using the Feynman-clock method, discussed in Sec. IV, the starting point is to use Eq. (15) to write the objective function in Eq. (14) as a real function, as required for implementation on D-Wave's QA,

$$F^{(\mathcal{C})} = \sum_{\alpha\beta}\big(a_{\alpha}^{\mathrm{Re}}a_{\beta}^{\mathrm{Re}}\mathcal{C}_{\alpha\beta}^{\mathrm{Re}} - a_{\alpha}^{\mathrm{Re}}a_{\beta}^{\mathrm{Im}}\mathcal{C}_{\alpha\beta}^{\mathrm{Im}} + a_{\alpha}^{\mathrm{Im}}a_{\beta}^{\mathrm{Re}}\mathcal{C}_{\alpha\beta}^{\mathrm{Im}} + a_{\alpha}^{\mathrm{Im}}a_{\beta}^{\mathrm{Im}}\mathcal{C}_{\alpha\beta}^{\mathrm{Re}}\big). \quad \text{(A4)}$$

The rows and columns of the QUBO matrix are doubled in length to accommodate the real and imaginary parts of each coefficient $a_{\alpha} = a_{\alpha}^{\mathrm{Re}} + ia_{\alpha}^{\mathrm{Im}}$. This is accomplished simply by increasing the range of the i index from $[1, K]$ to $[1, 2K]$, with $1 \leqslant i \leqslant K$ used for a_{α}^{Re} and $(K+1) \leqslant i \leqslant 2K$ for a_{α}^{Im}. Obtaining the expression for the QUBO matrix associated with $F^{(\mathcal{C})}$ follows straightforwardly from its derivation given above for the corresponding QUBO matrix for eigenstates and energies. For example, the first term in Eq. (A4) is analogous to that in Eq. (6),

$$\sum_{\alpha\beta}a_{\alpha}^{\mathrm{Re}}a_{\beta}^{\mathrm{Re}}\mathcal{C}_{\alpha\beta}^{\mathrm{Re}} = \sum_{\alpha\beta}\sum_{i,j=1}^{K}\Big[2^{i+j-2K-2z}(-1)^{\delta_{iK}+\delta_{jK}}\mathcal{C}_{\alpha\beta}^{\mathrm{Re}} + 2\delta_{\alpha\beta}\delta_{ij}2^{i-K-z}(-1)^{\delta_{iK}}\sum_{\gamma}a_{\gamma}^{\mathrm{Re},(z)}\mathcal{C}_{\gamma\beta}^{\mathrm{Re}}\Big]q_i^{\alpha}q_j^{\beta}, \quad \text{(A5)}$$

where the sum over the indices i, j is over the range $[1, K]$. The last term in Eq. (A4) is also analogous, but with i, j summed over $[K+1, 2K]$,

$$\sum_{\alpha\beta}a_{\alpha}^{\mathrm{Im}}a_{\beta}^{\mathrm{Im}}\mathcal{C}_{\alpha\beta}^{\mathrm{Re}} = \sum_{\alpha\beta}\sum_{i,j=K+1}^{2K}\Big[2^{i'+j'-2K-2z}(-1)^{\delta_{i'K}+\delta_{j'K}}\mathcal{C}_{\alpha\beta}^{\mathrm{Re}} + 2\delta_{\alpha\beta}\delta_{i'j'}2^{i'-K-z}(-1)^{\delta_{i'K}}\sum_{\gamma}a_{\gamma}^{\mathrm{Im},(z)}\mathcal{C}_{\gamma\beta}^{\mathrm{Re}}\Big]q_i^{\alpha}q_j^{\beta}, \quad \text{(A6)}$$

where i' is defined by $i' \equiv i - K$.

For the second and third terms in Eq. (A4), we employ the same binary identity $q_i^{\alpha} = (q_i^{\alpha})^2$, but keep in mind that the indices i, j run over different values. For example, for the $a_{\alpha}^{\mathrm{Re}}a_{\beta}^{\mathrm{Im}}$ term,

$$-\sum_{\alpha\beta}a_{\alpha}^{\mathrm{Re}}a_{\beta}^{\mathrm{Im}}\mathcal{C}_{\alpha\beta}^{\mathrm{Im}} = -\sum_{\alpha\beta}\Bigg[\sum_{i=1}^{K}\sum_{j=K+1}^{2K}2^{i+j'-2K-2z}(-1)^{\delta_{iK}+\delta_{j'K}}\mathcal{C}_{\alpha\beta}^{\mathrm{Im}} + \sum_{i,j=K+1}^{2K}\delta_{\alpha\beta}\delta_{i'j'}2^{j'-K-z}(-1)^{\delta_{j'K}}\sum_{\gamma}a_{\gamma}^{\mathrm{Re},(z)}\mathcal{C}_{\gamma\beta}^{\mathrm{Im}} + \sum_{i,j=1}^{K}\delta_{\alpha\beta}\delta_{ij}2^{i-K-z}(-1)^{\delta_{iK}}\sum_{\gamma}a_{\gamma}^{\mathrm{Im},(z)}\mathcal{C}_{\alpha\gamma}^{\mathrm{Im}}\Bigg]q_i^{\alpha}q_j^{\beta}. \quad \text{(A7)}$$

TABLE VII. Vacuum-to-vacuum probability $|\langle 00|\hat{U}_t|00\rangle|^2$ and energy in the electric field $\langle\hat{\mathcal{H}}_E\rangle$ of the one-plaquette system, as shown in Fig. 10, with $K = 2$ and $N_A = 10^3$. The uncertainties correspond to 68% confidence intervals determined from $N_{\mathrm{run}} = 20$ independent runs.

δt	t	$\lvert\langle 00\rvert\hat{U}_t\lvert 00\rangle\rvert^2$	$\langle\hat{\mathcal{H}}_E\rangle$
0.2	0	0.999988^{+10}_{-46}	$(0.6^{+2.5}_{-0.5}) \times 10^{-4}$
0.2	0.2	0.9802^{+13}_{-3}	0.0537^{+43}_{-14}
0.2	0.4	0.9271^{+23}_{-6}	0.2018^{+97}_{-33}
0.5	0	0.999956^{+42}_{-64}	$(2.0^{+4.2}_{-1.8}) \times 10^{-4}$
0.5	0.5	0.8921^{+47}_{-42}	0.3030^{+95}_{-71}
0.5	1.0	0.7139^{+66}_{-56}	0.828^{+34}_{-20}
0.7	0	0.99995^{+3}_{-81}	$(0.3^{+4.4}_{-0.2}) \times 10^{-3}$
0.7	0.7	0.816^{+7}_{-20}	0.535^{+85}_{-14}
0.7	1.4	0.6750^{+78}_{-51}	0.903^{+45}_{-20}
0.9	0	0.99999^{+1}_{-13}	$(0.9^{+7.9}_{-0.8}) \times 10^{-4}$
0.9	0.9	0.7435^{+18}_{-66}	0.738^{+11}_{-8}
0.9	1.8	0.768^{+2}_{-11}	0.645^{+34}_{-9}
1.1	0	0.999980^{+17}_{-68}	$(0.9^{+4.4}_{-0.7}) \times 10^{-4}$
1.1	1.1	0.6949^{+91}_{-21}	0.877^{+8}_{-21}
1.1	2.2	0.9239^{+20}_{-20}	0.226^{+7}_{-10}
1.3	0	0.99990^{+9}_{-73}	$(0.4^{+4.1}_{-0.3}) \times 10^{-3}$
1.3	1.3	0.670^{+5}_{-26}	0.926^{+93}_{-17}
1.3	2.6	0.995^{+2}_{-13}	0.025^{+76}_{-9}

TABLE VIII. The (raw) probability of flavor transitions $P_i(t)$ and single-neutrino entanglement entropy $S_i(t)$, as shown in Fig. 11, with $K = 2$ and $N_A = 10^3$. The uncertainties correspond to 68% confidence intervals determined from $N_{\text{run}} = 20$ independent runs.

δt	t	$P_1(t)$	$P_2(t)$	$P_3(t)$	$P_4(t)$	$S_1(t)$	$S_2(t)$	$S_3(t)$	$S_4(t)$
1.1	0	0.0065^{+36}_{-11}	0.0073^{+48}_{-26}	0.0053^{+27}_{-34}	0.0054^{+46}_{-18}	0.052^{+15}_{-8}	0.054^{+40}_{-16}	0.041^{+19}_{-21}	0.044^{+33}_{-10}
1.1	1.1	0.163^{+26}_{-15}	0.121^{+31}_{-8}	0.144^{+22}_{-18}	0.200^{+24}_{-19}	0.420^{+54}_{-52}	0.277^{+95}_{-80}	0.211^{+36}_{-86}	0.408^{+38}_{-75}
2.2	0	0.0092^{+50}_{-31}	0.0077^{+27}_{-21}	0.0062^{+28}_{-33}	0.0070^{+15}_{-27}	0.071^{+25}_{-23}	0.057^{+23}_{-17}	0.051^{+23}_{-25}	0.056^{+6}_{-19}
2.2	2.2	0.276^{+30}_{-61}	0.143^{+22}_{-23}	0.159^{+23}_{-23}	0.285^{+53}_{-32}	0.785^{+68}_{-74}	0.413^{+72}_{-90}	0.334^{+143}_{-64}	0.746^{+67}_{-59}
3.3	0	0.0054^{+31}_{-25}	0.0057^{+37}_{-21}	0.0057^{+36}_{-24}	0.0067^{+29}_{-36}	0.041^{+7}_{-18}	0.042^{+33}_{-10}	0.049^{+19}_{-21}	0.051^{+25}_{-20}
3.3	3.3	0.407^{+21}_{-21}	0.095^{+25}_{-13}	0.101^{+21}_{-12}	0.411^{+31}_{-20}	0.953^{+18}_{-15}	0.426^{+100}_{-37}	0.431^{+68}_{-50}	0.958^{+14}_{-10}
4.4	0	0.0078^{+32}_{-29}	0.0075^{+15}_{-39}	0.0056^{+14}_{-18}	0.0058^{+8}_{-22}	0.058^{+19}_{-16}	0.059^{+8}_{-27}	0.043^{+10}_{-14}	0.048^{+4}_{-14}
4.4	4.4	0.542^{+47}_{-26}	0.212^{+24}_{-27}	0.240^{+26}_{-32}	0.559^{+45}_{-44}	0.961^{+17}_{-36}	0.569^{+100}_{-42}	0.575^{+75}_{-65}	0.968^{+13}_{-46}
5.5	0	0.0088^{+71}_{-41}	0.0092^{+37}_{-44}	0.0060^{+52}_{-24}	0.0066^{+28}_{-30}	0.051^{+55}_{-14}	0.058^{+26}_{-26}	0.051^{+32}_{-24}	0.043^{+25}_{-12}
5.5	5.5	0.727^{+36}_{-29}	0.229^{+23}_{-35}	0.234^{+76}_{-29}	0.737^{+32}_{-40}	0.760^{+41}_{-51}	0.715^{+59}_{-73}	0.670^{+110}_{-83}	0.752^{+99}_{-18}
6.6	0	0.0085^{+46}_{-35}	0.0086^{+55}_{-41}	0.0092^{+37}_{-26}	0.0092^{+38}_{-33}	0.064^{+19}_{-23}	0.066^{+26}_{-28}	0.059^{+20}_{-15}	0.067^{+27}_{-20}
6.6	6.6	0.782^{+26}_{-29}	0.201^{+56}_{-42}	0.220^{+41}_{-26}	0.782^{+41}_{-44}	0.727^{+50}_{-77}	0.695^{+61}_{-101}	0.703^{+69}_{-93}	0.741^{+62}_{-85}
7.7	0	0.0123^{+73}_{-60}	0.0133^{+69}_{-56}	0.0066^{+53}_{-35}	0.0083^{+22}_{-43}	0.087^{+41}_{-33}	0.082^{+46}_{-27}	0.054^{+39}_{-26}	0.051^{+23}_{-14}
7.7	7.7	0.665^{+29}_{-46}	0.326^{+42}_{-53}	0.286^{+57}_{-28}	0.632^{+45}_{-60}	0.873^{+30}_{-33}	0.803^{+87}_{-103}	0.750^{+41}_{-63}	0.895^{+51}_{-34}
8.8	0	0.009^{+13}_{-4}	0.0083^{+67}_{-34}	0.0081^{+69}_{-49}	0.0065^{+68}_{-31}	0.065^{+45}_{-25}	0.059^{+24}_{-16}	0.055^{+49}_{-27}	0.053^{+39}_{-24}
8.8	8.8	0.606^{+41}_{-42}	0.280^{+25}_{-24}	0.273^{+33}_{-22}	0.603^{+61}_{-57}	0.945^{+32}_{-47}	0.813^{+37}_{-32}	0.793^{+44}_{-41}	0.939^{+27}_{-42}
9.9	0	0.0104^{+49}_{-28}	0.0106^{+66}_{-29}	0.0106^{+24}_{-43}	0.0106^{+45}_{-40}	0.078^{+23}_{-20}	0.079^{+34}_{-25}	0.075^{+16}_{-24}	0.077^{+28}_{-27}
9.9	9.9	0.455^{+39}_{-72}	0.298^{+51}_{-73}	0.246^{+99}_{-36}	0.422^{+76}_{-45}	0.954^{+16}_{-38}	0.834^{+57}_{-107}	0.787^{+106}_{-85}	0.949^{+30}_{-24}

TABLE IX. Probability of flavor transitions $P_i(t)$ and single-neutrino entanglement entropy $S_i(t)$, as shown in Fig. 11, with $K = 2$ and $N_A = 10^3$, after two steps of the iterative procedure. The uncertainties correspond to 68% confidence intervals determined from $N_{\text{run}} = 20$ independent runs.

δt	t	$P_1(t)$	$P_2(t)$	$P_3(t)$	$P_4(t)$	$S_1(t)$	$S_2(t)$	$S_3(t)$	$S_4(t)$
1.1	0	$0.00013\ ^{+11}_{-7}$	$0.00015\ ^{+6}_{-7}$	$0.00010\ ^{+9}_{-3}$	$0.00011\ ^{+8}_{-4}$	$0.0018\ ^{+12}_{-9}$	$0.0020\ ^{+8}_{-8}$	$0.0013\ ^{+11}_{-4}$	$0.0013\ ^{+10}_{-4}$
1.1	1.1	$0.1553\ ^{+35}_{-27}$	$0.1205\ ^{+25}_{-29}$	$0.1242\ ^{+44}_{-24}$	$0.1586\ ^{+39}_{-36}$	$0.3154\ ^{+92}_{-146}$	$0.0843\ ^{+102}_{-94}$	$0.0832\ ^{+100}_{-75}$	$0.3143\ ^{+69}_{-82}$
2.2	0	$0.00013\ ^{+4}_{-5}$	$0.00012\ ^{+13}_{-6}$	$0.00008\ ^{+4}_{-5}$	$0.00011\ ^{+8}_{-4}$	$0.0016\ ^{+5}_{-7}$	$0.0015\ ^{+11}_{-7}$	$0.0011\ ^{+5}_{-6}$	$0.0014\ ^{+7}_{-5}$
2.2	2.2	$0.2610\ ^{+47}_{-42}$	$0.1240\ ^{+23}_{-53}$	$0.1256\ ^{+29}_{-54}$	$0.2639\ ^{+32}_{-60}$	$0.7437\ ^{+132}_{-88}$	$0.2377\ ^{+32}_{-96}$	$0.2397\ ^{+128}_{-84}$	$0.7408\ ^{+76}_{-67}$
3.3	0	$0.00007\ ^{+7}_{-4}$	$0.00007\ ^{+9}_{-4}$	$0.00009\ ^{+5}_{-4}$	$0.00008\ ^{+3}_{-3}$	$0.0009\ ^{+8}_{-4}$	$0.0010\ ^{+9}_{-5}$	$0.0012\ ^{+8}_{-4}$	$0.0010\ ^{+4}_{-3}$
3.3	3.3	$0.4159\ ^{+31}_{-14}$	$0.0811\ ^{+13}_{-34}$	$0.0810\ ^{+25}_{-24}$	$0.4164\ ^{+22}_{-22}$	$0.9785\ ^{+16}_{-11}$	$0.3958\ ^{+70}_{-119}$	$0.3933\ ^{+102}_{-85}$	$0.9788\ ^{+16}_{-14}$
4.4	0	$0.00013\ ^{+5}_{-3}$	$0.00012\ ^{+10}_{-4}$	$0.00010\ ^{+5}_{-3}$	$0.00010\ ^{+9}_{-4}$	$0.0018\ ^{+5}_{-8}$	$0.0016\ ^{+11}_{-6}$	$0.0012\ ^{+6}_{-3}$	$0.0014\ ^{+9}_{-5}$
4.4	4.4	$0.5871\ ^{+72}_{-51}$	$0.2185\ ^{+38}_{-47}$	$0.2185\ ^{+45}_{-58}$	$0.5859\ ^{+48}_{-67}$	$0.9593\ ^{+31}_{-28}$	$0.5328\ ^{+100}_{-83}$	$0.5325\ ^{+159}_{-73}$	$0.9603\ ^{+43}_{-46}$
5.5	0	$0.00010\ ^{+6}_{-4}$	$0.00011\ ^{+6}_{-3}$	$0.00009\ ^{+6}_{-3}$	$0.00014\ ^{+7}_{-4}$	$0.0013\ ^{+5}_{-4}$	$0.0014\ ^{+3}_{-4}$	$0.0013\ ^{+8}_{-4}$	$0.0017\ ^{+4}_{-8}$
5.5	5.5	$0.7174\ ^{+35}_{-61}$	$0.2088\ ^{+45}_{-29}$	$0.2101\ ^{+17}_{-48}$	$0.7202\ ^{+50}_{-33}$	$0.7996\ ^{+53}_{-34}$	$0.6434\ ^{+80}_{-93}$	$0.6396\ ^{+57}_{-72}$	$0.7967\ ^{+72}_{-69}$
6.6	0	$0.00011\ ^{+9}_{-6}$	$0.00013\ ^{+7}_{-6}$	$0.00011\ ^{+9}_{-3}$	$0.00013\ ^{+7}_{-7}$	$0.0016\ ^{+7}_{-8}$	$0.0016\ ^{+7}_{-7}$	$0.0013\ ^{+7}_{-5}$	$0.0017\ ^{+10}_{-8}$
6.6	6.6	$0.7846\ ^{+36}_{-28}$	$0.1996\ ^{+17}_{-48}$	$0.2012\ ^{+57}_{-41}$	$0.7843\ ^{+49}_{-49}$	$0.7339\ ^{+78}_{-61}$	$0.7041\ ^{+87}_{-94}$	$0.7057\ ^{+117}_{-80}$	$0.7356\ ^{+105}_{-65}$
7.7	0	$0.00014\ ^{+4}_{-6}$	$0.00014\ ^{+4}_{-7}$	$0.00006\ ^{+7}_{-2}$	$0.00010\ ^{+3}_{-6}$	$0.0017\ ^{+6}_{-6}$	$0.0018\ ^{+4}_{-8}$	$0.0009\ ^{+7}_{-3}$	$0.0013\ ^{+4}_{-7}$
7.7	7.7	$0.6550\ ^{+42}_{-48}$	$0.2978\ ^{+37}_{-44}$	$0.2911\ ^{+54}_{-48}$	$0.6510\ ^{+44}_{-70}$	$0.8612\ ^{+60}_{-52}$	$0.7497\ ^{+88}_{-89}$	$0.7477\ ^{+56}_{-93}$	$0.8592\ ^{+62}_{-66}$
8.8	0	$0.00009\ ^{+10}_{-2}$	$0.00012\ ^{+5}_{-4}$	$0.00011\ ^{+7}_{-5}$	$0.00010\ ^{+8}_{-5}$	$0.0012\ ^{+9}_{-4}$	$0.0015\ ^{+7}_{-5}$	$0.0013\ ^{+9}_{-6}$	$0.0012\ ^{+11}_{-5}$
8.8	8.8	$0.5607\ ^{+58}_{-53}$	$0.2562\ ^{+40}_{-52}$	$0.2540\ ^{+48}_{-29}$	$0.5614\ ^{+68}_{-46}$	$0.9881\ ^{+15}_{-36}$	$0.7755\ ^{+63}_{-90}$	$0.7732\ ^{+75}_{-82}$	$0.9874\ ^{+18}_{-30}$
9.9	0	$0.00011\ ^{+6}_{-7}$	$0.00011\ ^{+8}_{-6}$	$0.00009\ ^{+6}_{-4}$	$0.00008\ ^{+11}_{-4}$	$0.0015\ ^{+8}_{-8}$	$0.0015\ ^{+8}_{-8}$	$0.0012\ ^{+5}_{-5}$	$0.0011\ ^{+16}_{-4}$
9.9	9.9	$0.3740\ ^{+36}_{-34}$	$0.2593\ ^{+40}_{-41}$	$0.2576\ ^{+70}_{-45}$	$0.3740\ ^{+29}_{-36}$	$0.9464\ ^{+37}_{-23}$	$0.7991\ ^{+143}_{-47}$	$0.7980\ ^{+136}_{-38}$	$0.9466\ ^{+27}_{-22}$

TABLE X. The (raw) logarithmic negativity for the different neutrino pairs $\mathcal{N}_{ij}(t)$, as shown in Fig. 12, with $K = 2$ and $N_A = 10^3$. The uncertainties correspond to 68% confidence intervals determined from $N_{\text{run}} = 20$ independent runs.

δt	t	$\mathcal{N}_{12}(t)$	$\mathcal{N}_{13}(t)$	$\mathcal{N}_{14}(t)$	$\mathcal{N}_{23}(t)$	$\mathcal{N}_{24}(t)$	$\mathcal{N}_{34}(t)$
1.1	0	0.107^{+32}_{-29}	0.063^{+44}_{-42}	0.053^{+52}_{-33}	0.048^{+44}_{-32}	0.078^{+62}_{-47}	0.054^{+13}_{-20}
1.1	1.1	0.212^{+64}_{-134}	0.128^{+61}_{-83}	0.417^{+98}_{-95}	0.073^{+70}_{-56}	0.186^{+99}_{-116}	0.045^{+70}_{-27}
2.2	0	0.103^{+67}_{-23}	0.068^{+97}_{-37}	0.088^{+39}_{-49}	0.048^{+49}_{-30}	0.046^{+46}_{-37}	0.028^{+46}_{-17}
2.2	2.2	0.078^{+137}_{-69}	0.238^{+130}_{-110}	0.611^{+103}_{-51}	0.071^{+69}_{-70}	0.215^{+56}_{-47}	0.026^{+10}_{-22}
3.3	0	0.056^{+34}_{-26}	0.033^{+45}_{-16}	0.038^{+48}_{-27}	0.049^{+44}_{-35}	0.064^{+78}_{-43}	0.085^{+44}_{-36}
3.3	3.3	0.063^{+87}_{-12}	0.194^{+43}_{-47}	0.735^{+24}_{-31}	0.068^{+76}_{-59}	0.197^{+43}_{-33}	0.071^{+42}_{-32}
4.4	0	0.120^{+31}_{-38}	0.057^{+36}_{-21}	0.045^{+22}_{-12}	0.066^{+9}_{-28}	0.036^{+25}_{-23}	0.052^{+56}_{-25}
4.4	4.4	0.143^{+19}_{-88}	0.188^{+23}_{-68}	0.637^{+64}_{-52}	0.133^{+127}_{-77}	0.142^{+42}_{-46}	0.126^{+124}_{-74}
5.5	0	0.089^{+57}_{-33}	0.062^{+56}_{-47}	0.059^{+62}_{-38}	0.051^{+44}_{-39}	0.064^{+54}_{-43}	0.042^{+30}_{-29}
5.5	5.5	0.365^{+60}_{-106}	0.058^{+29}_{-36}	0.361^{+38}_{-196}	0.220^{+57}_{-93}	0.053^{+19}_{-53}	0.349^{+55}_{-109}
6.6	0	0.056^{+67}_{-32}	0.062^{+29}_{-18}	0.074^{+102}_{-53}	0.078^{+39}_{-47}	0.081^{+42}_{-41}	0.075^{+49}_{-53}
6.6	6.6	0.321^{+66}_{-157}	0.000^{+27}_{-0}	0.363^{+66}_{-200}	0.285^{+92}_{-102}	0.000^{+28}_{-0}	0.303^{+75}_{-65}
7.7	0	0.146^{+96}_{-43}	0.047^{+29}_{-34}	0.061^{+33}_{-44}	0.042^{+58}_{-19}	0.055^{+40}_{-23}	0.040^{+36}_{-29}
7.7	7.7	0.006^{+68}_{-6}	0	0.631^{+57}_{-58}	0.513^{+84}_{-128}	0	0.000^{+67}_{-0}
8.8	0	0.076^{+49}_{-33}	0.056^{+48}_{-36}	0.072^{+33}_{-35}	0.083^{+60}_{-59}	0.065^{+46}_{-32}	0.031^{+43}_{-18}
8.8	8.8	0.000^{+86}_{-0}	0	0.766^{+56}_{-52}	0.663^{+50}_{-46}	0	0
9.9	0	0.088^{+45}_{-43}	0.069^{+45}_{-43}	0.067^{+90}_{-27}	0.076^{+20}_{-49}	0.071^{+43}_{-28}	0.068^{+61}_{-50}
9.9	9.9	0	0	0.837^{+47}_{-76}	0.718^{+100}_{-87}	0.000^{+28}_{-0}	0

Collecting together the contributions, the following QUBO matrix for the Feynman clock is obtained:

$$Q_{\alpha,i;\beta,j} = \begin{cases} 2^{i+j-2K-2z}(-1)^{\delta_{iK}+\delta_{jK}}\mathcal{C}^{\text{Re}}_{\alpha\beta} \\ \quad + \delta_{\alpha\beta}\delta_{ij}2^{i-K-z}(-1)^{\delta_{iK}}\sum_\gamma \left(2a^{\text{Re},(z)}_\gamma \mathcal{C}^{\text{Re}}_{\gamma\beta} - a^{\text{Im},(z)}_\gamma \mathcal{C}^{\text{Im}}_{\alpha\gamma} + a^{\text{Im},(z)}_\gamma \mathcal{C}^{\text{Im}}_{\gamma\beta}\right), & 1 \leqslant i, j \leqslant K \\ -2^{i+j'-2K-2z}(-1)^{\delta_{iK}+\delta_{j'K}}\mathcal{C}^{\text{Im}}_{\alpha\beta}, & 1 \leqslant i, j' \leqslant K \\ 2^{i'+j-2K-2z}(-1)^{\delta_{i'K}+\delta_{jK}}\mathcal{C}^{\text{Im}}_{\alpha\beta}, & 1 \leqslant i', j \leqslant K \\ 2^{i'+j'-2K-2z}(-1)^{\delta_{i'K}+\delta_{j'K}}\mathcal{C}^{\text{Re}}_{\alpha\beta} \\ \quad + \delta_{\alpha\beta}\delta_{i'j'}2^{i'-K-z}(-1)^{\delta_{i'K}}\sum_\gamma \left(2a^{\text{Im},(z)}_\gamma \mathcal{C}^{\text{Re}}_{\gamma\beta} - a^{\text{Re},(z)}_\gamma \mathcal{C}^{\text{Im}}_{\gamma\beta} + a^{\text{Re},(z)}_\gamma \mathcal{C}^{\text{Im}}_{\alpha\gamma}\right), & 1 \leqslant i', j' \leqslant K. \end{cases} \tag{A8}$$

This can be somewhat simplified because $\mathcal{C}^{\text{Im}}_{\alpha\beta}$ is antisymmetric while $\mathcal{C}^{\text{Re}}_{\alpha\beta}$ is symmetric, leading to the expressions given in Eq. (15),

$$Q_{\alpha,i;\beta,j} = \begin{cases} 2^{i+j-2K-2z}(-1)^{\delta_{iK}+\delta_{jK}}\mathcal{C}^{\text{Re}}_{\alpha\beta} + 2\delta_{\alpha\beta}\delta_{ij}2^{i-K-z}(-1)^{\delta_{iK}}\sum_\gamma \left(a^{\text{Re},(z)}_\gamma \mathcal{C}^{\text{Re}}_{\gamma\beta} + a^{\text{Im},(z)}_\gamma \mathcal{C}^{\text{Im}}_{\gamma\beta}\right), & 1 \leqslant i, j \leqslant K \\ -2^{i+j'-2K-2z}(-1)^{\delta_{iK}+\delta_{j'K}}\mathcal{C}^{\text{Im}}_{\alpha\beta}, & 1 \leqslant i, j' \leqslant K \\ 2^{i'+j-2K-2z}(-1)^{\delta_{i'K}+\delta_{jK}}\mathcal{C}^{\text{Im}}_{\alpha\beta}, & 1 \leqslant i', j \leqslant K \\ 2^{i'+j'-2K-2z}(-1)^{\delta_{i'K}+\delta_{j'K}}\mathcal{C}^{\text{Re}}_{\alpha\beta} + 2\delta_{\alpha\beta}\delta_{i'j'}2^{i'-K-z}(-1)^{\delta_{i'K}}\sum_\gamma \left(a^{\text{Im},(z)}_\gamma \mathcal{C}^{\text{Re}}_{\gamma\beta} - a^{\text{Re},(z)}_\gamma \mathcal{C}^{\text{Im}}_{\gamma\beta}\right), & 1 \leqslant i', j' \leqslant K. \end{cases} \tag{A9}$$

APPENDIX B: MORE ON OUR RESULTS

The (average) time it takes to perform $N_A = 10^3$ anneals on both the neal simulator and Advantage for the HO and AHO Hamiltonians for a single zoom step from Sec. III is reported in Table III. Regarding the time specific to the quantum processor, it takes into account two separate steps. The first one is the programming time, during which the values of the QUBO matrix are transferred to the quantum processor (same for all problem sizes, 8–15 ms). The next step is the annealing phase, repeated N_A times, which is further decomposed into three steps: the annealing time ($t_A = 20$ μs), the readout time (size dependent, varying between 100 and 200 μs), and the delay time (the same for all problem sizes, 20.54 μs), during which the system is allowed to cool and reinitialized. For Advantage, the time spent finding the embedding should also be taken into account (although this part is not computed on the quantum processor, but locally); therefore its contribution is shown in a separate column.

Although the time required to find the configuration with minimum energy is around an order of magnitude smaller for Advantage than neal (increasing t_A would reduce this difference), the overhead time spent computing the embedding (not needed for the simulator) inverts the situation. As mentioned in Sec. III B, the embedding can be reused for the multiple zoom steps. This is possible because the required connectivity

TABLE XI. Logarithmic negativity for the different neutrino pairs $\mathcal{N}_{ij}(t)$, as shown in Fig. 12, with $K = 2$ and $N_A = 10^3$, after two steps of the iterative procedure. The uncertainties correspond to 68% confidence intervals determined from $N_{\text{run}} = 20$ independent runs.

δt	t	$\mathcal{N}_{12}(t)$	$\mathcal{N}_{13}(t)$	$\mathcal{N}_{14}(t)$	$\mathcal{N}_{23}(t)$	$\mathcal{N}_{24}(t)$	$\mathcal{N}_{34}(t)$
1.1	0	0.0164^{+66}_{-70}	0.0085^{+76}_{-50}	0.0068^{+40}_{-41}	0.0073^{+49}_{-25}	0.0069^{+83}_{-53}	0.0063^{+39}_{-33}
1.1	1.1	0.0015^{+48}_{-13}	0.1948^{+133}_{-114}	0.4851^{+66}_{-109}	0.0420^{+181}_{-124}	0.1945^{+150}_{-134}	0.0007^{+6}_{-7}
2.2	0	0.0089^{+99}_{-30}	0.0053^{+51}_{-24}	0.0076^{+53}_{-35}	0.0053^{+62}_{-17}	0.0077^{+97}_{-29}	0.0070^{+73}_{-17}
2.2	2.2	0.0173^{+36}_{-17}	0.2683^{+143}_{-75}	0.7316^{+41}_{-61}	0.0649^{+136}_{-166}	0.2650^{+61}_{-81}	0.0190^{+17}_{-34}
3.3	0	0.0051^{+46}_{-23}	0.0058^{+44}_{-22}	0.0027^{+59}_{-10}	0.0064^{+49}_{-38}	0.0036^{+47}_{-19}	0.0089^{+74}_{-43}
3.3	3.3	0.0847^{+53}_{-40}	0.2495^{+110}_{-48}	0.7827^{+86}_{-56}	0.0816^{+65}_{-169}	0.2515^{+68}_{-53}	0.0851^{+37}_{-33}
4.4	0	0.0154^{+72}_{-23}	0.0076^{+68}_{-37}	0.0076^{+43}_{-42}	0.0071^{+36}_{-25}	0.0075^{+39}_{-38}	0.0065^{+73}_{-41}
4.4	4.4	0.2013^{+127}_{-91}	0.1805^{+93}_{-56}	0.6847^{+68}_{-37}	0.1563^{+163}_{-113}	0.1816^{+66}_{-66}	0.2038^{+164}_{-103}
5.5	0	0.0066^{+25}_{-20}	0.0088^{+26}_{-34}	0.0101^{+38}_{-57}	0.0054^{+62}_{-29}	0.0105^{+91}_{-50}	0.0074^{+76}_{-35}
5.5	5.5	0.3155^{+137}_{-97}	0.0869^{+25}_{-38}	0.4790^{+114}_{-81}	0.2623^{+54}_{-83}	0.0888^{+18}_{-54}	0.3076^{+147}_{-101}
6.6	0	0.0082^{+56}_{-52}	0.0081^{+64}_{-44}	0.0107^{+95}_{-60}	0.0105^{+25}_{-43}	0.0101^{+44}_{-61}	0.0070^{+79}_{-31}
6.6	6.6	0.2342^{+173}_{-125}	0	0.4603^{+115}_{-182}	0.4220^{+59}_{-81}	0	0.2423^{+142}_{-126}
7.7	0	0.0174^{+39}_{-55}	0.0066^{+54}_{-37}	0.0077^{+40}_{-49}	0.0076^{+54}_{-25}	0.0091^{+34}_{-69}	0.0073^{+38}_{-25}
7.7	7.7	0	0	0.7085^{+89}_{-42}	0.6158^{+61}_{-87}	0	0
8.8	0	0.0088^{+27}_{-63}	0.0066^{+69}_{-31}	0.0082^{+34}_{-37}	0.0065^{+48}_{-34}	0.0076^{+60}_{-44}	0.0070^{+65}_{-37}
8.8	8.8	0	0	0.8992^{+20}_{-25}	0.7624^{+42}_{-47}	0	0
9.9	0	0.0098^{+119}_{-55}	0.0054^{+32}_{-26}	0.0073^{+26}_{-41}	0.0065^{+51}_{-22}	0.0082^{+33}_{-21}	0.0071^{+64}_{-27}
9.9	9.9	0	0	0.9397^{+20}_{-34}	0.8554^{+66}_{-48}	0	0

between the different logic qubits does not change; only the entries of the QUBO matrix change. More specifically, looking at Eq. (6), the additional term obtained from the zooming is added in the diagonal part of the QUBO matrix, where $\alpha = \beta$ and $i = j$ [the same argument can be used for Eq. (15)]. Table III does not take into account the time spent building the QUBO matrix or analyzing the results, since these steps are the same for both cases.

All of the results shown in the main text can be found in HDF5 format [185] in the file `SSMQA_data.h5`, where each set is labeled by the figure number, with additional metadata to specify the parameters used during its production and the dimension of the array (like the value of N_{run} or the number of zoom levels). For the results related to Figs. 10–12, only the compound states $|\Psi_t\rangle|t\rangle$ are included.

Additionally, in the following tables we provide the values plotted in the figures from the main text. The results shown in Figs. 6 and 7 are given in Table IV. The results shown in Fig. 8 are given in Table V. The results shown in Fig. 9 are given in Table VI The results shown in Fig. 10 are given in Table VII.The results shown in Fig. 11 are given in Tables VIII (raw results) and IX (after two steps of the iterative procedure) and the results shown in Fig. 12 are given in Tables X (raw results) and XI (after two steps of the iterative procedure).

[1] R. Landauer, Irreversibility and heat generation in the computing process, IBM J. Res. Dev. **5**, 183 (1961).

[2] C. H. Bennett, Logical reversibility of computation, IBM J. Res. Dev. **17**, 525 (1973).

[3] P. Benioff, The computer as a physical system: A microscopic quantum mechanical Hamiltonian model of computers as represented by Turing machines, J. Stat. Phys. **22**, 563 (1980).

[4] Y. I. Manin, *Computable and Uncomputable* (Sovetskoye Radio, Moscow,1980).

[5] R. P. Feynman, Simulating physics with computers, Int. J. Theor. Phys. **21**, 467 (1982).

[6] E. Fredkin and T. Toffoli, Conservative logic, Int. J. Theor. Phys. **21**, 219 (1982).

[7] R. P. Feynman, Quantum mechanical computers, Found. Phys. **16**, 507 (1986).

[8] R. Landauer, Information is physical, Phys. Today **44**(5), 23 (1991).

[9] J. Preskill, Quantum Computing in the NISQ era and beyond, Quantum **2**, 79 (2018).

[10] M. C. Bañuls, R. Blatt, J. Catani, A. Celi, J. I. Cirac, M. Dalmonte, L. Fallani, K. Jansen, M. Lewenstein, S. Montangero, C. A. Muschik, B. Reznik, E. Rico, L. Tagliacozzo, K. Van Acoleyen, F. Verstraete, U.-J. Wiese, M. Wingate, J. Zakrzewski, and P. Zoller, Simulating lattice gauge theories within quantum technologies, Eur. Phys. J. D **74**, 165 (2020).

[11] Y. Alexeev, D. Bacon, K. R. Brown, R. Calderbank, L. D. Carr, F. T. Chong, B. DeMarco, D. Englund, E. Farhi, B. Fefferman, A. V. Gorshkov, A. Houck, J. Kim, S. Kimmel, M. Lange, S. Lloyd, M. D. Lukin, D. Maslov, P. Maunz, C. Monroe *et al.*, Quantum computer systems for scientific discovery, PRX Quantum **2**, 017001 (2021).

[12] N. Klco, A. Roggero, and M. J. Savage, Standard model physics and the digital quantum revolution: Thoughts about the interface, Rep. Prog. Phys. **85**, 064301 (2022)

[13] A. B. Finnila, M. A. Gomez, C. Sebenik, C. Stenson, and J. D. Doll, Quantum annealing: A new method for minimizing multidimensional functions, Chem. Phys. Lett. **219**, 343 (1994).

[14] T. Kadowaki and H. Nishimori, Quantum annealing in the transverse Ising model, Phys. Rev. E **58**, 5355 (1998).

[15] E. Farhi, J. Goldstone, S. Gutmann, and M. Sipser, Quantum computation by adiabatic evolution, arXiv:quant-ph/0001106.

[16] E. Farhi, J. Goldstone, S. Gutmann, J. Lapan, A. Lundgren, and D. Preda, A quantum adiabatic evolution algorithm applied to random instances of an NP-complete problem, Science **292**, 472 (2001).

[17] M. Johnson, M. Amin, S. Gildert, T. Lanting, F. Hamze, N. Dickson, R. Harris, A. Berkley, J. Johansson, P. Bunyk, E. Chapple, C. Enderud, J. Hilton, K. Karimi, E. Ladizinsky, N. Ladizinsky, T. Oh, I. Perminov, C. Rich, and G. Rose, Quantum annealing with manufactured spins, Nature (London) **473**, 194 (2011).

[18] *D-Wave, QPU-Specific Physical Properties: Advantage_system4.1* (D-Wave Systems Inc., Burnaby, 2021).

[19] R. Harris, T. Lanting, A. J. Berkley, J. Johansson, M. W. Johnson, P. Bunyk, E. Ladizinsky, N. Ladizinsky, T. Oh, and S. Han, Compound Josephson-junction coupler for flux qubits with minimal crosstalk, Phys. Rev. B **80**, 052506 (2009).

[20] S. Boixo, T. F. Rønnow, S. Isakov, Z. Wang, D. Wecker, D. Lidar, J. Martinis, and M. Troyer, Evidence for quantum annealing with more than one hundred qubits, Nat. Phys. **10**, 218 (2014).

[21] J. A. Smolin and G. Smith, Classical signature of quantum annealing, Front. Phys. **2**, 52 (2014).

[22] D. Venturelli, D. J. J. Marchand, and G. Rojo, Proceedings of the 26th International Conference on Automated Planning and Scheduling, London, 2016, arXiv:1506.08479.

[23] F. Neukart, G. Compostella, C. Seidel, D. von Dollen, S. Yarkoni, and B. Parney, Traffic flow optimization using a quantum annealer, Front. ICT **4**, 29 (2017).

[24] N. T. T. Nguyen, G. T. Kenyon, and B. Yoon, A regression algorithm for accelerated lattice QCD that exploits sparse inference on the D-Wave quantum annealer, Sci. Rep. **10**, 10915 (2020).

[25] H. Irie, H. Liang, T. Doi, S. Gongyo, and T. Hatsuda, Hybrid quantum annealing via molecular dynamics, Sci. Rep. **11**, 8426 (2021).

[26] A. Mott, J. Job, J.-R. Vlimant, D. Lidar, and M. Spiropulu, Solving a Higgs optimization problem with quantum annealing for machine learning, Nature (London) **550**, 375 (2017).

[27] S. Das, A. J. Wildridge, S. B. Vaidya, and A. Jung, Track clustering with a quantum annealer for primary vertex reconstruction at hadron colliders, arXiv:1903.08879.

[28] H. Neven, V. S. Denchev, G. Rose, and W. G. Macready, Training a binary classifier with the quantum adiabatic algorithm, arXiv:0811.0416.

[29] K. L. Pudenz and D. A. Lidar, Quantum adiabatic machine learning, Quantum Inf. Process. **12**, 2027 (2013).

[30] V. S. Denchev, N. Ding, S. V. N. Vishwanathan, and H. Neven, in *Proceedings of the 29th International Conference on Machine Learning*, Edinburgh, 2012, arXiv:1205.1148.

[31] B. O'Gorman, R. Babbush, A. Perdomo-Ortiz, A. Aspuru-Guzik, and V. Smelyanskiy, Bayesian network structure learning using quantum annealing, Eur. Phys. J.: Spec. Top. **224**, 163 (2015).

[32] S. H. Adachi and M. P. Henderson, Application of quantum annealing to training of deep neural networks, arXiv:1510.06356.

[33] M. Benedetti, J. Realpe-Gómez, R. Biswas, and A. Perdomo-Ortiz, Estimation of effective temperatures in quantum annealers for sampling applications: A case study with possible applications in deep learning, Phys. Rev. A **94**, 022308 (2016).

[34] M. H. Amin, E. Andriyash, J. Rolfe, B. Kulchytskyy, and R. Melko, Quantum Boltzmann Machine, Phys. Rev. X **8**, 021050 (2018).

[35] D. Crawford, A. Levit, N. Ghadermarzy, J. S. Oberoi, and P. Ronagh, Reinforcement learning using quantum Boltzmann machines, Quantum Inf. Comput. **18**, 51 (2018).

[36] A. Perdomo-Ortiz, M. Benedetti, J. Realpe-Gómez, and R. Biswas, Opportunities and challenges for quantum-assisted machine learning in near-term quantum computers, Quantum Sci. Technol. **3**, 030502 (2018).

[37] J. Caldeira, J. Job, S. H. Adachi, B. Nord, and G. N. Perdue, Restricted Boltzmann machines for galaxy morphology classification with a quantum annealer, arXiv:1911.06259.

[38] W. Vinci, L. Buffoni, H. Sadeghi, A. Khoshaman, E. Andriyash, and M. H. Amin, A path towards quantum advantage in training deep generative models with quantum annealers, Mach. Learn.: Sci. Technol. **1**, 045028 (2019).

[39] L. Rocutto, C. Destri, and E. Prati, Quantum semantic learning by reverse annealing an adiabatic quantum computer, Adv. Quantum Technol. **4**, 2000133 (2021).

[40] V. Dixit, R. Selvarajan, M. A. Alam, T. S. Humble, and S. Kais, Training restricted Boltzmann machines with a D-Wave quantum annealer, Front. Phys. **9**, 589626 (2021).

[41] B. Gardas, J. Dziarmaga, W. H. Zurek, and M. Zwolak, Defects in quantum computers, Sci. Rep. **8**, 4539 (2018).

[42] R. Harris, Y. Sato, A. Berkley, M. Reis, F. Altomare, M. Amin, K. Boothby, P. Bunyk, C. Deng, C. Enderud, S. Huang, E. Hoskinson, M. Johnson, E. Ladizinsky, N. Ladizinsky, T. Lanting, R. Li, T. Medina, R. Molavi, and J. Yao, Phase transitions in a programmable quantum spin glass simulator, Science **361**, 162 (2018).

[43] A. D. King, J. Carrasquilla, J. Raymond, I. Ozfidan, E. Andriyash, A. Berkley, M. Reis, T. Lanting, R. Harris, F. Altomare, K. Boothby, P. I. Bunyk, C. Enderud, A. Fréchette, E. Hoskinson, N. Ladizinsky, T. Oh, G. Poulin-Lamarre, C. Rich, Y. Sato *et al.*, Observation of topological phenomena in a programmable lattice of 1,800 qubits, Nature (London) **560**, 456 (2018).

[44] P. Weinberg, M. Tylutki, J. M. Rönkkö, J. Westerholm, J. A. Åström, P. Manninen, P. Törmä, and A. W. Sandvik, Scaling and Diabatic Effects in Quantum Annealing with a D-Wave Device, Phys. Rev. Lett. **124**, 090502 (2020).

[45] A. D. King, J. Raymond, T. Lanting, S. V. Isakov, M. Mohseni, G. Poulin-Lamarre, S. Ejtemaee, W. Bernoudy, I. Ozfidan, A. Y. Smirnov, M. Reis, F. Altomare, M. Babcock, C. Baron, A. J. Berkley, K. Boothby, P. I. Bunyk, H. Christiani, C. Enderud, B. Evert *et al.*, Scaling advantage over path-integral Monte Carlo in quantum simulation of geometrically frustrated magnets, Nat. Commun. **12**, 1113 (2021).

[46] Y. Bando, Y. Susa, H. Oshiyama, N. Shibata, M. Ohzeki, F. J. Gómez-Ruiz, D. A. Lidar, S. Suzuki, A. del Campo, and H. Nishimori, Probing the universality of topological defect formation in a quantum annealer: Kibble-Zurek mechanism and beyond, Phys. Rev. Res. **2**, 033369 (2020).

[47] P. Kairys, A. D. King, I. Ozfidan, K. Boothby, J. Raymond, A. Banerjee, and T. S. Humble, Simulating the Shastry-Sutherland Ising model using quantum annealing, PRX Quantum **1**, 020320 (2020).

[48] T. Lanting, M. H. Amin, C. Baron, M. Babcock, J. Boschee, S. Boixo, V. N. Smelyanskiy, M. Foygel, and A. G. Petukhov, Probing environmental spin polarization with superconducting flux qubits, arXiv:2003.14244.

[49] K. Nishimura, H. Nishimori, and H. G. Katzgraber, Griffiths-McCoy singularity on the diluted Chimera graph: Monte Carlo simulations and experiments on quantum hardware, Phys. Rev. A **102**, 042403 (2020).

[50] A. D. King, C. Nisoli, E. D. Dahl, G. Poulin-Lamarre, and A. Lopez-Bezanilla, Qubit spin ice, Science **373**, 576 (2021).

[51] A. D. King, S. Suzuki, J. Raymond, A. Zucca, T. Lanting, F. Altomare, A. J. Berkley, S. Ejtemaee, E. Hoskinson, S. Huang, E. Ladizinsky, A. J. R. MacDonald, G. Marsden, T. Oh, G. Poulin-Lamarre, M. Reis, C. Rich, Y. Sato, J. D. Whittaker, J. Yao *et al.*, Coherent quantum annealing in a programmable 2000-qubit Ising chain, Nat. Phys. **18**, 1324 (2022).

[52] M. Hernandez, A. Zaribafiyan, M. Aramon, and M. Naghibi, A novel graph-based approach for determining molecular similarity, arXiv:1601.06693.

[53] M. Hernandez and M. Aramon, Enhancing quantum annealing performance for the molecular similarity problem, Quantum Inf. Process. **16**, 133 (2017).

[54] R. Xia, T. Bian, and S. Kais, Electronic structure calculations and the Ising Hamiltonian, J. Phys. Chem. B **122**, 3384 (2018).

[55] A. Teplukhin, B. K. Kendrick, and D. Babikov, Calculation of molecular vibrational spectra on a quantum annealer, J. Chem. Theory Comput. **15**, 4555 (2019).

[56] A. Teplukhin, B. K. Kendrick, S. Tretiak, and P. A. Dub, Electronic structure with direct diagonalization on a D-Wave quantum annealer, Sci. Rep. **10**, 20753 (2020).

[57] A. Teplukhin, B. K. Kendrick, S. M. Mniszewski, Y. Zhang, A. Kumar, C. F. A. Negre, P. M. Anisimov, S. Tretiak, and P. A. Dub, Computing molecular excited states on a D-Wave quantum annealer, Sci. Rep. **11**, 18796 (2021).

[58] A. Perdomo, C. Truncik, I. Tubert-Brohman, G. Rose, and A. Aspuru-Guzik, Construction of model Hamiltonians for adiabatic quantum computation and its application to finding low-energy conformations of lattice protein models, Phys. Rev. A **78**, 012320 (2008).

[59] A. Perdomo-Ortiz, N. Dickson, M. Drew-Brook, G. Rose, and A. Aspuru-Guzik, Finding low-energy conformations of lattice protein models by quantum annealing, Sci. Rep. **2**, 571 (2012).

[60] R. Y. Li, R. Di Felice, R. Rohs, and D. A. Lidar, Quantum annealing versus classical machine learning applied to a simplified computational biology problem, npj Quantum Inf. **4**, 14 (2018).

[61] T. Babej, C. Ing, and M. Fingerhuth, Coarse-grained lattice protein folding on a quantum annealer, arXiv:1811.00713.

[62] G. Rosenberg, P. Haghnegahdar, P. Goddard, P. Carr, K. Wu, and M. L. de Prado, Solving the optimal trading trajectory problem using a quantum annealer, IEEE J. Sel. Top. Signal Process. **10**, 1053 (2016).

[63] E. Grant, T. S. Humble, and B. Stump, Benchmarking Quantum Annealing Controls with Portfolio Optimization, Phys. Rev. Appl. **15**, 014012 (2021).

[64] A. Bouland, W. van Dam, H. Joorati, I. Kerenidis, and A. Prakash, Prospects and challenges of quantum finance, arXiv:2011.06492.

[65] K. Zick, O. Shehab, and M. French, Experimental quantum annealing: Case study involving the graph isomorphism problem, Sci. Rep. **5**, 11168 (2015).

[66] H. Ushijima-Mwesigwa, C. F. A. Negre, and S. M. Mniszewski, in *Proceedings of the Second International Workshop on Post Moores Era Supercomputing* (Association for Computing Machinery, New York, 2017), pp. 22–29.

[67] D. Vert, R. Sirdey, and S. Louise, Benchmarking quantum annealing against "hard" instances of the bipartite matching problem, SN Comput. Sci. **2**, 106 (2021).

[68] S. Ramos-Calderer, C. Bravo-Prieto, R. Lin, E. Bellini, M. Manzano, N. Aaraj, and J. I. Latorre, Solving systems of boolean multivariate equations with quantum annealing, Phys. Rev. Res. **4**, 013096 (2022).

[69] C. C. Chang, C.-C. Chen, C. Koerber, T. S. Humble, and J. Ostrowski, Integer programming from quantum annealing and open quantum systems, arXiv:2009.11970.

[70] C. C. Chang, A. Gambhir, T. S. Humble, and S. Sota, Quantum annealing for systems of polynomial equations, Sci. Rep. **9**, 10258 (2019).

[71] G. Schaller and R. Schützhold, The role of symmetries in adiabatic quantum algorithms, Quantum Inf. Comput. **10**, 109 (2010).

[72] X. Peng, Z. Liao, N. Xu, G. Qin, X. Zhou, D. Suter, and J. Du, Quantum Adiabatic Algorithm for Factorization and Its Experimental Implementation, Phys. Rev. Lett. **101**, 220405 (2008).

[73] N. Xu, J. Zhu, D. Lu, X. Zhou, X. Peng, and J. Du, Quantum Factorization of 143 on a Dipolar-Coupling Nuclear Magnetic Resonance System, Phys. Rev. Lett. **108**, 130501 (2012).

[74] R. Dridi and H. Alghassi, Prime factorization using quantum annealing and computational algebraic geometry, Sci. Rep. **7**, 43048 (2017).

[75] M. Maezawa, K. Imafuku, M. Hidaka, H. Koike, and S. Kawabata, in *Proceedings of the 16th International Superconductive Electronics Conference, Sorrento, 2017* (IEEE, Piscataway, 2017), pp. 1–3.

[76] S. Jiang, K. A. Britt, A. J. McCaskey, T. S. Humble, and S. Kais, Quantum annealing for prime factorization, Sci. Rep. **8**, 17667 (2018).

[77] S. A Rahman, R. Lewis, E. Mendicelli, and S. Powell, SU(2) lattice gauge theory on a quantum annealer, Phys. Rev. D **104**, 034501 (2021).

[78] J. R. McClean, J. A. Parkhill, and A. Aspuru-Guzik, Feynman's clock, a new variational principle, and parallel-in-time quantum dynamics, Proc. Natl. Acad. Sci. USA **110**, E3901 (2013).

[79] C. Cîrstoiu, Z. Holmes, J. Iosue, L. Cincio, P. J. Coles, and A. Sornborger, Variational fast forwarding for quantum simulation beyond the coherence time, npj Quantum Inf. **6**, 82 (2020).

[80] A. Ciavarella, N. Klco, and M. J. Savage, Trailhead for quantum simulation of SU(3) Yang-Mills lattice gauge theory in the local multiplet basis, Phys. Rev. D **103**, 094501 (2021).

[81] B. Hall, A. Roggero, A. Baroni, and J. Carlson, Simulation of collective neutrino oscillations on a quantum computer, Phys. Rev. D **104**, 063009 (2021).

[82] *D-Wave System Documentation* (D-Wave Systems Inc., Burnaby, 2022).

[83] A. Zlokapa, A. Mott, J. Job, J.-R. Vlimant, D. Lidar, and M. Spiropulu, Quantum adiabatic machine learning by zooming into a region of the energy surface, Phys. Rev. A **102**, 062405 (2020).

[84] See Supplemental Material at http://link.aps.org/supplemental/10.1103/PhysRevA.106.052605 for the practical implementation of these and subsequent algorithms.

[85] A. Pearson, A. Mishra, I. Hen, and D. A. Lidar, Analog errors in quantum annealing: Doom and hope, npj Quantum Inf. **5**, 107 (2019).

[86] T. Zaborniak and R. de Sousa, Benchmarking Hamiltonian noise in the D-Wave quantum annealer, IEEE Trans. Quantum Eng. **2**, 1 (2021).

[87] H. Oshiyama and M. Ohzeki, Benchmark of quantum-inspired heuristic solvers for quadratic unconstrained binary optimization, Sci. Rep. **12**, 2146 (2022).

[88] *Ocean Software Documentation* (D-Wave Systems Inc., Burnaby, 2021).

[89] N. Klco and M. J. Savage, Minimally entangled state preparation of localized wave functions on quantum computers, Phys. Rev. A **102**, 012612 (2020).

[90] S. P. Jordan, H. Krovi, K. S. M. Lee, and J. Preskill, BQP-completeness of scattering in scalar quantum field theory, Quantum **2**, 44 (2018).

[91] S. P. Jordan, K. S. M. Lee, and J. Preskill, Quantum computation of scattering in scalar quantum field theories, Quantum Inf. Comput. **14**, 1014 (2014).

[92] S. P. Jordan, K. S. M. Lee, and J. Preskill, Quantum algorithms for quantum field theories, Science **336**, 1130 (2012).

[93] S. P. Jordan, K. S. M. Lee, and J. Preskill, Quantum algorithms for fermionic quantum field theories, arXiv:1404.7115.

[94] N. Klco and M. J. Savage, Digitization of scalar fields for quantum computing, Phys. Rev. A **99**, 052335 (2019).

[95] R. D. Somma, Quantum simulations of one dimensional quantum systems, Quantum Inf. Comput. **16**, 1125 (2016).

[96] A. Macridin, P. Spentzouris, J. Amundson, and R. Harnik, Electron-Phonon Systems on a Universal Quantum Computer, Phys. Rev. Lett. **121**, 110504 (2018).

[97] A. Macridin, P. Spentzouris, J. Amundson, and R. Harnik, Digital quantum computation of fermion-boson interacting systems, Phys. Rev. A **98**, 042312 (2018).

[98] A. Macridin, A. C. Y. Li, S. Mrenna, and P. Spentzouris, Bosonic field digitization for quantum computers, Phys. Rev. A **105**, 052405 (2022).

[99] G. Van Rossum and F. L. Drake, *Python 3 Reference Manual* (CreateSpace, Scotts Valley, 2009).

[100] F. Pérez and B. E. Granger, IPython: A system for interactive scientific computing, Comput. Sci. Eng. **9**, 21 (2007).

[101] *Mathematica* (Wolfram Research, Inc., Champaign, 2022), Version 12.3.10.

[102] T. Blum, T. Izubuchi, and E. Shintani, New class of variance-reduction techniques using lattice symmetries, Phys. Rev. D **88**, 094503 (2013).

[103] E. Shintani, R. Arthur, T. Blum, T. Izubuchi, C. Jung, and C. Lehner, Covariant approximation averaging, Phys. Rev. D **91**, 114511 (2015).

[104] A. Brandt, Multi-level adaptive solutions to boundary-value problems, Math. Comput. **31**, 333 (1977).

[105] *D-Wave Leap* (D-Wave Systems Inc., Burnaby, 2022).

[106] J. Cai, W. G. Macready, and A. Roy, A practical heuristic for finding graph minors, arXiv:1406.2741.

[107] D. G. Tempel and A. Aspuru-Guzik, The Kitaev–Feynman clock for open quantum systems, New J. Phys. **16**, 113066 (2014).

[108] R. P. Feynman, Quantum mechanical computers, Opt. News **11**, 11 (1985).

[109] A. Y. Kitaev, A. Shen, and M. N. Vyalyi, *Classical and Quantum Computation* (American Mathematical Society, Providence, 2002), Vol. 47.

[110] K. Jałowiecki, A. Więckowski, P. Gawron, and B. Gardas, Parallel in time dynamics with quantum annealers, Sci. Rep. **10**, 13534 (2020).

[111] A. Teplukhin, B. K. Kendrick, and D. Babikov, Solving complex eigenvalue problems on a quantum annealer with applications to quantum scattering resonances, Phys. Chem. Chem. Phys. **22**, 26136 (2020).

[112] T. Byrnes and Y. Yamamoto, Simulating lattice gauge theories on a quantum computer, Phys. Rev. A **73**, 022328 (2006).

[113] E. Zohar and B. Reznik, Confinement and Lattice Quantum-Electrodynamic Electric Flux Tubes Simulated with Ultracold Atoms, Phys. Rev. Lett. **107**, 275301 (2011).

[114] E. Zohar, J. I. Cirac, and B. Reznik, Simulating Compact Quantum Electrodynamics with Ultracold Atoms: Probing Confinement and Nonperturbative Effects, Phys. Rev. Lett. **109**, 125302 (2012).

[115] L. Tagliacozzo, A. Celi, A. Zamora, and M. Lewenstein, Optical Abelian lattice gauge theories, Ann. Phys. (NY) **330**, 160 (2013).

[116] E. Zohar, J. I. Cirac, and B. Reznik, Simulating (2+1)-Dimensional Lattice QED with Dynamical Matter Using Ultracold Atoms, Phys. Rev. Lett. **110**, 055302 (2013).

[117] E. Zohar, J. I. Cirac, and B. Reznik, Cold-Atom Quantum Simulator for SU(2) Yang-Mills Lattice Gauge Theory, Phys. Rev. Lett. **110**, 125304 (2013).

[118] P. Hauke, D. Marcos, M. Dalmonte, and P. Zoller, Quantum Simulation of a Lattice Schwinger Model in a Chain of Trapped Ions, Phys. Rev. X **3**, 041018 (2013).

[119] U.-J. Wiese, Ultracold quantum gases and lattice systems: Quantum simulation of lattice gauge theories, Ann. Phys. (Berlin) **525**, 777 (2013).

[120] D. Marcos, P. Widmer, E. Rico, M. Hafezi, P. Rabl, U. J. Wiese, and P. Zoller, Two-dimensional lattice gauge theories with superconducting quantum circuits, Ann. Phys. (NY) **351**, 634 (2014).

[121] Y. Kuno, K. Kasamatsu, Y. Takahashi, I. Ichinose, and T. Matsui, Real-time dynamics and proposal for feasible experiments of lattice gauge–Higgs model simulated by cold atoms, New J. Phys. **17**, 063005 (2015).

[122] A. Bazavov, Y. Meurice, S.-W. Tsai, J. Unmuth-Yockey, and J. Zhang, Gauge-invariant implementation of the Abelian Higgs model on optical lattices, Phys. Rev. D **92**, 076003 (2015).

[123] V. Kasper, F. Hebenstreit, M. Oberthaler, and J. Berges, Schwinger pair production with ultracold atoms, Phys. Lett. B **760**, 742 (2016).

[124] G. K. Brennen, G. Pupillo, E. Rico, T. M. Stace, and D. Vodola, Loops and Strings in a Superconducting Lattice Gauge Simulator, Phys. Rev. Lett. **117**, 240504 (2016).

[125] E. A. Martinez, C. A. Muschik, P. Schindler, D. Nigg, A. Erhard, M. Heyl, P. Hauke, M. Dalmonte, T. Monz, P. Zoller, and R. Blatt, Real-time dynamics of lattice gauge theories with a few-qubit quantum computer, Nature (London) **534**, 516 (2016).

[126] Y. Kuno, S. Sakane, K. Kasamatsu, I. Ichinose, and T. Matsui, Atomic quantum simulation of a three-dimensional U(1) gauge-Higgs model, Phys. Rev. A **94**, 063641 (2016).

[127] E. Zohar, A. Farace, B. Reznik, and J. I. Cirac, Digital lattice gauge theories, Phys. Rev. A **95**, 023604 (2017).

[128] V. Kasper, F. Hebenstreit, F. Jendrzejewski, M. K. Oberthaler, and J. Berges, Implementing quantum electrodynamics with ultracold atomic systems, New J. Phys. **19**, 023030 (2017).

[129] C. Muschik, M. Heyl, E. Martinez, T. Monz, P. Schindler, B. Vogell, M. Dalmonte, P. Hauke, R. Blatt, and P. Zoller, U(1) Wilson lattice gauge theories in digital quantum simulators, New J. Phys. **19**, 103020 (2017).

[130] D. González-Cuadra, E. Zohar, and J. I. Cirac, Quantum simulation of the Abelian-Higgs lattice gauge theory with ultracold atoms, New J. Phys. **19**, 063038 (2017).

[131] M. C. Bañuls, K. Cichy, J. I. Cirac, K. Jansen, and S. Kühn, Efficient Basis formulation for $(1+1)$-Dimensional SU(2) Lattice Gauge Theory: Spectral Calculations with Matrix Product States, Phys. Rev. X **7**, 041046 (2017).

[132] N. Klco, E. F. Dumitrescu, A. J. McCaskey, T. D. Morris, R. C. Pooser, M. Sanz, E. Solano, P. Lougovski, and M. J. Savage, Quantum-classical computation of Schwinger model dynamics using quantum computers, Phys. Rev. A **98**, 032331 (2018).

[133] D. B. Kaplan and J. R. Stryker, Gauss's law, duality, and the Hamiltonian formulation of U(1) lattice gauge theory, Phys. Rev. D **102**, 094515 (2020).

[134] H.-H. Lu, N. Klco, J. M. Lukens, T. D. Morris, A. Bansal, A. Ekström, G. Hagen, T. Papenbrock, A. M. Weiner, M. J. Savage, and P. Lougovski, Simulations of subatomic many-body physics on a quantum frequency processor, Phys. Rev. A **100**, 012320 (2019).

[135] J. R. Stryker, Oracles for Gauss's law on digital quantum computers, Phys. Rev. A **99**, 042301 (2019).

[136] Z. Davoudi, M. Hafezi, C. Monroe, G. Pagano, A. Seif, and A. Shaw, Towards analog quantum simulations of lattice gauge theories with trapped ions, Phys. Rev. Res. **2**, 023015 (2020).

[137] N. Klco, M. J. Savage, and J. R. Stryker, SU(2) non-Abelian gauge field theory in one dimension on digital quantum computers, Phys. Rev. D **101**, 074512 (2020).

[138] G. Magnifico, M. Dalmonte, P. Facchi, S. Pascazio, F. V. Pepe, and E. Ercolessi, Real time dynamics and confinement in the $\mathbb{Z}_n$ Schwinger-Weyl lattice model for 1+1 QED, Quantum **4**, 281 (2020).

[139] D. Luo, J. Shen, M. Highman, B. K. Clark, B. DeMarco, A. X. El-Khadra, and B. Gadway, Framework for simulating gauge theories with dipolar spin systems, Phys. Rev. A **102**, 032617 (2020).

[140] A. F. Shaw, P. Lougovski, J. R. Stryker, and N. Wiebe, Quantum algorithms for simulating the lattice Schwinger model, Quantum **4**, 306 (2020).

[141] J. C. Halimeh, H. Lang, J. Mildenberger, Z. Jiang, and P. Hauke, Gauge-symmetry protection using single-body terms, PRX Quantum **2**, 040311 (2021).

[142] D. Paulson, L. Dellantonio, J. F. Haase, A. Celi, A. Kan, A. Jena, C. Kokail, R. van Bijnen, K. Jansen, P. Zoller, and C. A. Muschik, Towards simulating 2D effects in lattice gauge theories on a quantum computer, PRX Quantum **2**, 030334 (2021).

[143] J. C. Halimeh, V. Kasper, and P. Hauke, Fate of lattice gauge theories under decoherence, arXiv:2009.07848.

[144] M. Van Damme, J. C. Halimeh, and P. Hauke, Gauge-symmetry violation quantum phase transition in lattice gauge theories, arXiv:2010.07338.

[145] R. Ott, T. V. Zache, F. Jendrzejewski, and J. Berges, Scalable Cold-Atom Quantum Simulator for Two-Dimensional QED, Phys. Rev. Lett. **127**, 130504 (2021).

[146] Y. Y. Atas, J. Zhang, R. Lewis, A. Jahanpour, J. F. Haase, and C. A. Muschik, SU(2) hadrons on a quantum computer via a variational approach, Nat. Commun. **12**, 6499 (2021).

[147] Z. Davoudi, N. M. Linke, and G. Pagano, Toward simulating quantum field theories with controlled phonon-ion dynamics: A hybrid analog-digital approach, Phys. Rev. Res. **3**, 043072 (2021).

[148] A. Kan, L. Funcke, S. Kühn, L. Dellantonio, J. Zhang, J. F. Haase, C. A. Muschik, and K. Jansen, Investigating a $(3+1)$D topological θ-term in the Hamiltonian formulation of lattice gauge theories for quantum and classical simulations, Phys. Rev. D **104**, 034504 (2021).

[149] J. R. Stryker, Shearing approach to gauge invariant Trotterization, arXiv:2105.11548.

[150] M. Aidelsburger, L. Barbiero, A. Bermudez, T. Chanda, A. Dauphin, D. González-Cuadra, P. R. Grzybowski, S. Hands, F. Jendrzejewski, J. Jünemann, G. Juzeliūnas, V. Kasper, A. Piga, S.-J. Ran, M. Rizzi, G. Sierra, L. Tagliacozzo, E. Tirrito, T. V. Zache, J. Zakrzewski *et al.*, Cold atoms meet lattice gauge theory, Philos. Trans. R. Soc. A **380**, 20210064 (2021).

[151] A. N. Ciavarella and I. A. Chernyshev, Preparation of the SU(3) Lattice Yang-Mills vacuum with variational quantum methods, Phys. Rev. D **105**, 074504 (2022).

[152] J. Kogut and L. Susskind, Hamiltonian formulation of Wilson's lattice gauge theories, Phys. Rev. D **11**, 395 (1975).

[153] J. B. Kogut, An introduction to lattice gauge theory and spin systems, Rev. Mod. Phys. **51**, 659 (1979).

[154] R. Brower, S. Chandrasekharan, and U. J. Wiese, QCD as a quantum link model, Phys. Rev. D **60**, 094502 (1999).

[155] D. Banerjee, M. Bögli, M. Dalmonte, E. Rico, P. Stebler, U. J. Wiese, and P. Zoller, Atomic Quantum Simulation of U(N) and SU(N) Non-Abelian Lattice Gauge Theories, Phys. Rev. Lett. **110**, 125303 (2013).

[156] L. Tagliacozzo, A. Celi, P. Orland, and M. Lewenstein, Simulations of non-Abelian gauge theories with optical lattices, Nat. Commun. **4**, 2615 (2013).

[157] U.-J. Wiese, From quantum link models to D-theory: a resource efficient framework for the quantum simulation and computation of gauge theories, Philos. Trans. R. Soc. A **380**, 20210068 (2021).

[158] A. Alexandru, P. F. Bedaque, S. Harmalkar, H. Lamm, S. Lawrence, and N. C. Warrington (NuQS Collaboration), Gluon field digitization for quantum computers, Phys. Rev. D **100**, 114501 (2019).

[159] Y. Ji, H. Lamm, and S. Zhu (NuQS Collaboration), Gluon field digitization via group space decimation for quantum computers, Phys. Rev. D **102**, 114513 (2020).

[160] M. Agostini, G. Benato, J. A. Detwiler, J. Menéndez, and F. Vissani, Toward the discovery of matter creation with neutrinoless double-beta decay, arXiv:2202.01787.

[161] M. J. Savage, R. A. Malaney, and G. M. Fuller, Neutrino oscillations and the leptonic charge of the universe, Astrophys. J. **368**, 1 (1991).

[162] J. Pantaleone, Neutrino oscillations at high densities, Phys. Lett. B **287**, 128 (1992).

[163] B. H. J. McKellar and M. J. Thomson, Oscillating neutrinos in the early universe, Phys. Rev. D **49**, 2710 (1994).

[164] Y. Z. Qian and G. M. Fuller, Neutrino-neutrino scattering and matter enhanced neutrino flavor transformation in supernovae, Phys. Rev. D **51**, 1479 (1995).

[165] F. Capozzi and N. Saviano, Neutrino flavor conversions in high-density astrophysical and cosmological environments, Universe **8**, 94 (2022).

[166] N. F. Bell, A. A. Rawlinson, and R. F. Sawyer, Speedup through entanglement: Many body effects in neutrino processes, Phys. Lett. B **573**, 86 (2003).

[167] A. Friedland and C. Lunardini, Do many particle neutrino interactions cause a novel coherent effect? J. High Energy Phys. 10 (2003) 043.

[168] R. F. Sawyer, "Classical" instabilities and "quantum" speed-up in the evolution of neutrino clouds, arXiv:hep-ph/0408265.

[169] Y. Pehlivan, A. B. Balantekin, T. Kajino, and T. Yoshida, Invariants of collective neutrino oscillations, Phys. Rev. D **84** (2011) 065008.

[170] H. Duan, G. M. Fuller, J. Carlson, and Y.-Z. Qian, Simulation of coherent nonlinear neutrino flavor transformation in the supernova environment: Correlated neutrino trajectories, Phys. Rev. D **74**, 105014 (2006).

[171] E. Rrapaj, Exact solution of multiangle quantum many-body collective neutrino-flavor oscillations, Phys. Rev. C **101**, 065805 (2020).

[172] M. J. Cervia, A. V. Patwardhan, A. B. Balantekin, S. N. Coppersmith, and C. W. Johnson, Entanglement and collective flavor oscillations in a dense neutrino gas, Phys. Rev. D **100**, 083001 (2019).

[173] A. Roggero, Entanglement and many-body effects in collective neutrino oscillations, Phys. Rev. D **104**, 103016 (2021).

[174] A. Roggero, Dynamical phase transitions in models of collective neutrino oscillations, Phys. Rev. D **104**, 123023 (2021).

[175] C. A. Argüelles and B. J. P. Jones, Neutrino oscillations in a quantum processor, Phys. Rev. Res. **1**, 033176 (2019).

[176] K. Yeter-Aydeniz, S. Bangar, G. Siopsis, and R. C. Pooser, Collective neutrino oscillations on a quantum computer, Quantum Inf. Process **21**, 84 (2022).

[177] M. J. Cervia, P. Siwach, A. V. Patwardhan, A. B. Balantekin, S. N. Coppersmith, and C. W. Johnson, Collective neutrino oscillations with tensor networks using a time-dependent variational principle, Phys. Rev. D **105**, 123025 (2022).

[178] J. D. Martin, A. Roggero, H. Duan, J. Carlson, and V. Cirigliano, Classical and quantum evolution in a simple coherent neutrino problem, Phys. Rev. D **105**, 083020 (2022).

[179] N. Chancellor, Domain wall encoding of discrete variables for quantum annealing and QAOA, Quantum Sci. Technol. **4**, 045004 (2019).

[180] S. Abel, N. Chancellor, and M. Spannowsky, Quantum computing for quantum tunneling, Phys. Rev. D **103**, 016008 (2021).

[181] N. Klco and M. J. Savage, Systematically localizable operators for quantum simulations of quantum field theories, Phys. Rev. A **102**, 012619 (2020).

[182] A. N. Ciavarella, S. Caspar, H. Singh, M. J. Savage, and P. Lougovski, Floquet engineering Heisenberg from Ising using constant drive fields for quantum simulation, arXiv:2207.09438.

[183] J. D. Hunter, Matplotlib: A 2D graphics environment, Comput. Sci. Eng. **9**, 90 (2007).

[184] *Anaconda Software Distribution* (Anaconda, Inc., Austin, 2020), Version 2-2.4.0.

[185] *Hierarchical Data Format* (The HDF Group, Champaign, 1997–2022), Version 5.